EQUIVALENT CIRCUIT MODELING AND SIGNAL INTEGRITY ANALYSIS OF

MAGNETO-STATIC RESPONSIVE STRUCTURES, AND THEIR APPLICATIONS IN

CHANGING THE EFFECTIVE PERMITTIVITY OF MICROSTRIP TRANSMISSION LINES

A Thesis
Submitted to the Graduate Faculty
of the
North Dakota State University
of Agriculture and Applied Science

By

Jacob Matthew Parrow

In Partial Fulfillment of the Requirements
for the Degree of
MASTER OF SCIENCE

Major Department:
Electrical and Computer Engineering

March 2016

Fargo, North Dakota

NORTH DAKOTA STATE UNIVERSITY

Graduate School

Title

EQUIVALENT CIRCUIT MODELING AND SIGNAL INTEGRITY ANALYSIS

OF MAGNETO-STATIC RESPONSIVE STRUCTURES, AND THEIR

APPLICATIONS IN CHANGING THE EFFECTIVE PERMITTIVITY OF

MICROSTRIP TRANSMISSION LINES

By

Jacob Matthew Parrow

The supervisory committee certifies that this thesis complies with North Dakota State University's regulations and meets the accepted standards for the degree of

MASTER OF SCIENCE

SUPERVISORY COMMITTEE:

Dr. Benjamin D. Braaten

Chair

Dr. David A. Rogers

Dr. Daniel L. Ewert

Dr. Nikita E. Barabanov

Approved:

1 April 2016

Date

Scott C. Smith

Department Chair

ABSTRACT

This work presents the equivalent circuit model, ringing and overshoot characteristics, as well as the ability of a new magneto-static responsive structure (MRS) to achieve the reconfigurability of a variable effective permittivity structure (VEPS). Through the use of a static magnetic field and micro-sized conductive magnetic particles, the MRS can be used to connect separate transmission lines (TL) that operate up to a radio frequency of 5 GHz. The simulated and measured results show the MRS functions well compared to other switching methods. The VEPS's ability to achieve effective permittivity reconfigurability is also demonstrated, showing that the VEPS functions as the well-known mushroom structure when the MRSs are in the on state and as a regular TL when the MRSs are in the off state. Finally, several brief studies of the MRS are performed, including the activation methods, MRS geometry, different types of magnetic particles, and smaller embedded MRSs within the VEPS.

ACKNOWLEDGEMENTS

DEDICATION

I dedicate this work to my wonderful fiance, Kelley, who I am so thankful for because of her faith,

patience, love, humor, and her great care for everyone.

TABLE OF CONTENTS

LIST OF TABLES

LIST OF FIGURES

LIST OF SYMBOLS

LIST OF APPENDIX FIGURES

1. INTRODUCTION

1.1. Statement of the Topic

Wireless technologies exist all around in the world today, whether it is the cell phone sitting in one's pocket, the Wi-Fi router sitting in their house, or the satellite dish sitting on their roof. Each of these technologies have been studied extensively and optimized to some degree, but there are still many optimizations to be made. Each of these technologies revolves around some sort of Radio Frequency (RF) switching method, which allows the wireless technology to turn on or off a certain signal. These RF switching methods include devices such as Pin diodes, micro-electromechanical systems (MEMS) and field effect transistors (FETs). Pin diodes require additional components or power such as a RF choke or minimum DC voltage to bias the diode [1] - [2], which leads to excess electrical noise around the system. MEMS switches can require high voltages and often involve moving mechanical parts, which is typically not desired [2, 3, 4, 5, 6, 7, 8] due to device fatigue. FETs also require extra power and are susceptible to overload voltages, thus requiring special handling during installation [9] - [10].
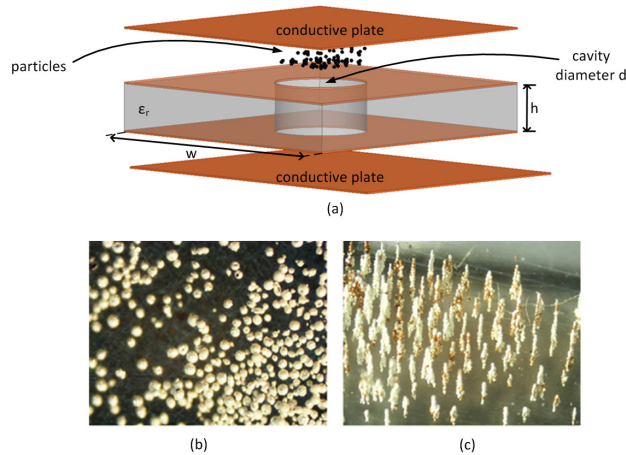
Figure 1.1. (a) The magneto-static responsive structure (MRS) (b) Particles without a magnetic field (off) state and (c) Particles with a magnetic field (on) state

To address these issues, the novel Magneto-static Responsive Structure (MRS) shown in Fig. 1.1(a) is proposed with an in-depth study on the MRS. The MRS consists of a small piece of

TMM4 substrate with a cavity drilled out of it. The cavity is then filled with silver coated magnetic micro size particles. When there is no magnetic field, the particles settle (Fig. 1.1(b)) and the MRS functions as a switch in the off state. But when magnetic field is introduced to the switch, the particles align vertically in the direction of the field lines (Fig. 1.1(c)) and stack to connect (on) the two conductive planes, allowing for implementation into most RF systems requiring a RF switching method.

1.2. Applications of RF Switching Methods

RF switches can be applied to a variety of designs for numerous reasons. One such reason is antenna reconfigurability. Multiple frequencies mean multiple antennas, meaning more space, power, and design time associated with each of those antennas. Antenna reconfigurability is the ability to change the properties of an antenna in a controlled and reversible manner, allowing a single antenna to function as several.

RF switches are also widely used in different microwave test systems for signal routing and devices under test (DUT). Incorporating a switch into a switch matrix system enables one to route signals from multiple instruments to single or multiple DUTs. This allows multiple tests to be performed with the same setup [11].

1.2.1. Pin Diodes

A Pin diode is a device that operates as a variable resistor at RF and microwave frequencies, with resistance varying from 1 Ω to 10 kΩ. This resistance is determined only by the forward biased DC current [11]. By adjusting the DC current, the Pin diode can function as a switch with high (off) and low (on) resistances as shown in Fig. 1.2.
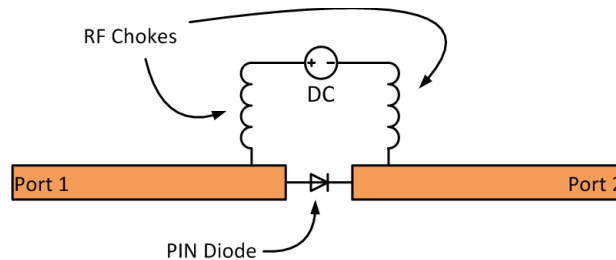
Figure 1.2. Typical setup for Pin diode when it is being used as a switch, to turn the switch on the DC source must maintain a minimum voltage.

Pin diodes have been studied extensively, whether it is characteristics of a particular structure [12], their use in high power switching [13], or even their use in antenna reconfigurability as presented in [14]. And while they possess many positive qualities, they still have their downfalls including biasing circuitry[15], extra components, and an inherently lossy nature.

1.2.2. Micro-Electromechanical Systems (MEMS)

Micro-electromechanical systems (MEMS) exist in many forms, one such would appear as a small robotic arm. Through the use of this arm, a small conductor could be attached between two separate transmission lines, connecting the lines (on). When the arm is moved, the lines are then disconnected (off) as shown in Fig. 1.3.
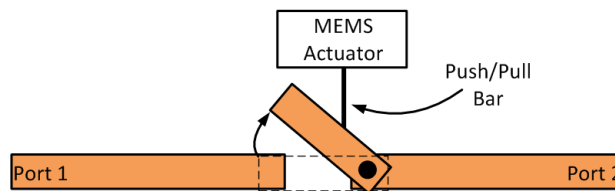
Figure 1.3. Typical setup for MEMS when it is being used as a switch, to turn the switch on, the MEMS actuator must push the bar connecting the two traces with the conductive connector.

As presented in numerous areas [2, 3, 7, 8], there is growing interest in using MEMS in several systems, especially areas such as antenna reconfigurability [4, 6] or integrated circuits [5]. However, MEMS often require moving parts, decreasing their reliability and lifespan in many systems. Due to their nature, they often require high voltages to operate and can require too much space to be used commercially.

1.3. Controlling the Phase and Effective Permittivity

Another important topic in the world of engineering is controlling the phase constant β and the effective permittivity ϵ_{reff} of a system. The β and ϵ_{reff} are directly related, so it is not possible to affect one without affecting the other. One such application could be a dual fed leaky-wave antenna, as shown in Fig. 1.4. Here, the meander line is used to introduce a 180 degree phase shift between two feed points using the same source, which is a common method for antennas that require separate feed points out of phase. However, sometimes the required length of meander line is too large to be implemented into the system. Leading to the use of phase controlling devices. One such device is the varactor diode, which can be used to adjust the phase of a line without
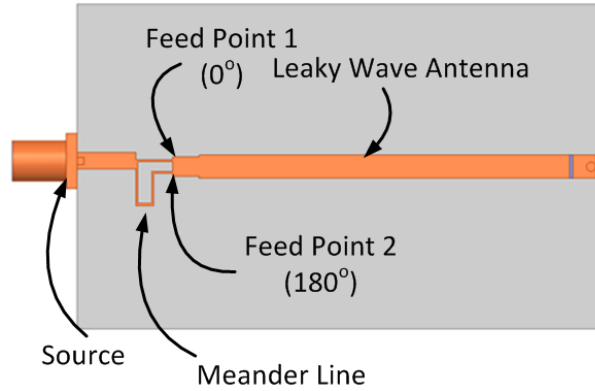
Figure 1.4. A meander line being used in a leaky wave antenna to introduce a 180 degree phase shift between separate feed points

adjusting the physical length of the line. One example of a varactor diode being used is found in [16], where the author uses varactor diodes as phase shifters to beam steer an antenna array.

Other work used to adjust the β with the primary purpose of adjusting the ϵ_{reff} is the well known mushroom structure, which utilizes a via to connect a conductive patch with either a reference plane or other conductive plane, a basic example of a mushroom structure can be seen in Fig. 1.5 where mushroom structures are being spaced underneath of a copper trace. In [17] the author studies wave interactions in a left-handed (LH) material with basic mushroom structures. In [18] the author studies the use of helical vias instead of the commonly used vertical via, the
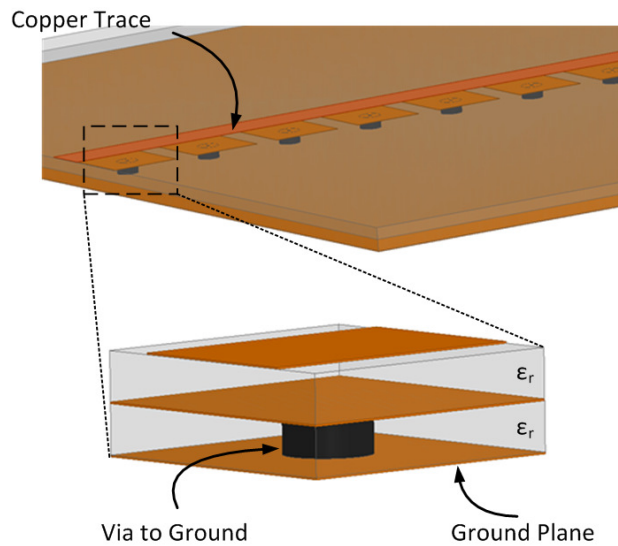
Figure 1.5. Mushroom structures being embedded within a substrate underneath a copper trace (above) with a unit cell view of the mushroom structure (below)

4
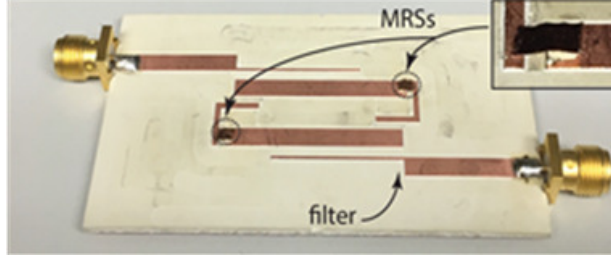
Figure 1.6. Reconfigurable band-pass filter as shown in [20]

author found that more than a 50% size reduction could be obtained by using the unique helical via. In [19] the author achieves different dual-band and dual-polarizations by allocating different frequencies to each polarization through the use of H-type mushroom structures, rather than the typical square mushroom structure. These are but a few of the studies revolving around mushroom structures.

1.4. Previous work

There has been little work done on the MRS. The work that has been done includes it's use for reconfiguring a filter, reconfiguring an antenna, and the general characterization of certain aspects of the switch and reed switches. In [20], the author demonstrates the MRS's ability to be used to reconfigure a band-pass microwave filter. Based on the design shown in [21], the author successfully replaced the Pin diodes in [21] with the MRS, as shown in Fig. 1.6. Then, the filter design was both simulated and measured, with comparable results. It can be seen in Fig. 1.7, that by activating and deactivating the MRSs, that the filter can successfully allow separate frequencies to pass while blocking the other. This design has multiple advantages over the design
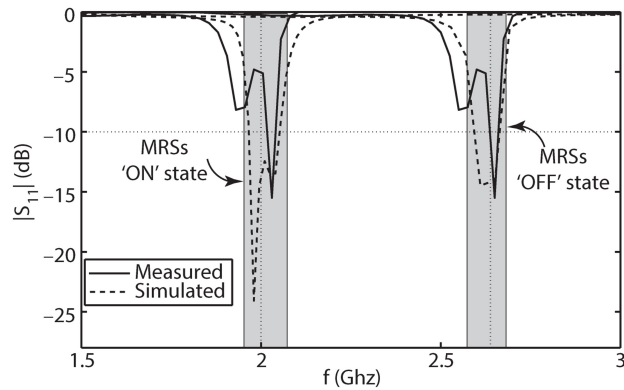
Figure 1.7. Reconfigurable band-pass filter $|S_{11}|$ with MRSs in the on and off states as shown in [20]

5
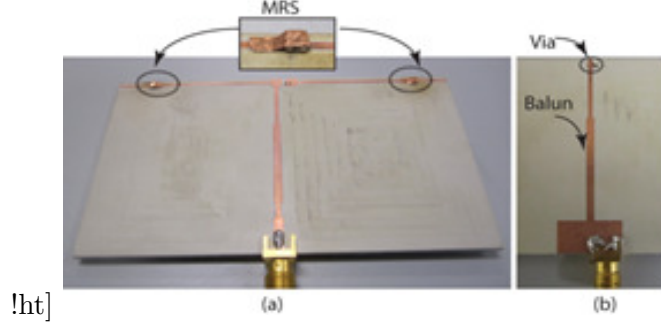
Figure 1.8. Manufactured reconfigurable dipole antenna top plane (a) and reference plane (b) as shown in [22]

presented in [21], including easier implementation, fewer components, and no biasing circuitry. The MRSs are seen again in [22] where they are used to reconfigure an antenna following the procedure in [23] - [24]. The dipole that was designed and manufactured in [22] can be seen in Fig. 1.8. Here, the author used MRSs to connect arms of the dipole with an additional transmission line, thus achieving different electrical lengths of the dipole when deactivating or activating the MRSs. By activating and deactivating the MRSs, the author achieved antenna reconfigurability for two separate frequencies, 1.5 GHz and 1.9 GHz. These results can be viewed in Fig. 1.9. While other switching methods could have been used here, the MRSs are shown to be an effective tool for achieving antenna reconfigurability, perhaps more effective than other switching methods.
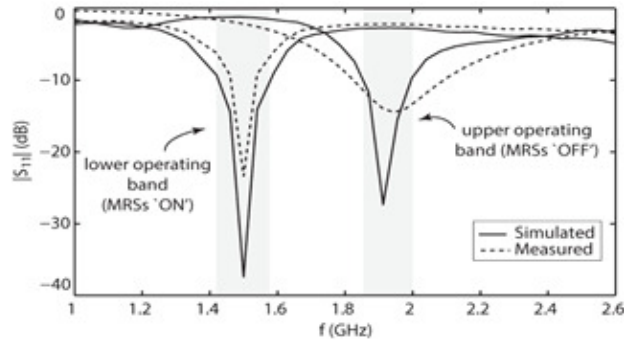
Figure 1.9. $|S_{11}|$ of the MRS reconfigurable dipole as shown in [22]

Finally, in [25] the author characterizes several important aspects of the MRS. They start off with an efficient simulating and manufacturing process, with an efficient manner in which to count the number of magnetic particles within the MRSs. Later they move onto a proposed lumped circuit model of the MRS, and eventually to several applications including antenna reconfigurability.

After reviewing previous work on the magneto-static responsive structure, it can be seen that very little work has been covered regarding this research. In this work, several contributions in an effort to expand the knowledge about the magneto-static responsive structures are proposed.

1.5. Contributions

The contributions of this research are: a more accurate lumped component model of the MRS accurate up to 3 GHz based on the model given in [25], ringing and overshoot characteristics of the MRS with a comparison to the regularly used Pin diode and a regular transmission line. And the MRS's ability to change the effective dielectric constant (ϵ_{reff}) through altering the phase constant β.

2. EQUIVALENT CIRCUIT MODELING OF THE MAGNETO-STATIC RESPONSIVE STRUCTURE

2.1. Introduction

2.2. Geometry of the Component

The MRS architecture is shown in Fig. 2.1. It consists of a double copper clad (cu) board of Rogers TMM4 material ($\epsilon_r = 4.5$) with a height H = 1.524 mm and width W = 50 mm. Then 50 Ω traces separated by a gap g = 0.3 mm are milled on the top plane. The MRS is designed from the same material, and consists of a height h = 0.508 mm and width w = 0.3 mm with a cavity diameter d = 0.9 mm drilled out of it. The MRS is then soldered onto the end of trace 1 of the discontinuous Transmission Line (TL), and then filled with silver coated magnetic micro size particles [26]. To finish the process, copper foil was placed on top of the MRS and secured with copper tape connecting the foil to trace 2. Copper foil was used to stop the particles from sticking directly to the tape, which would interrupt the process of turning the switch on or off.
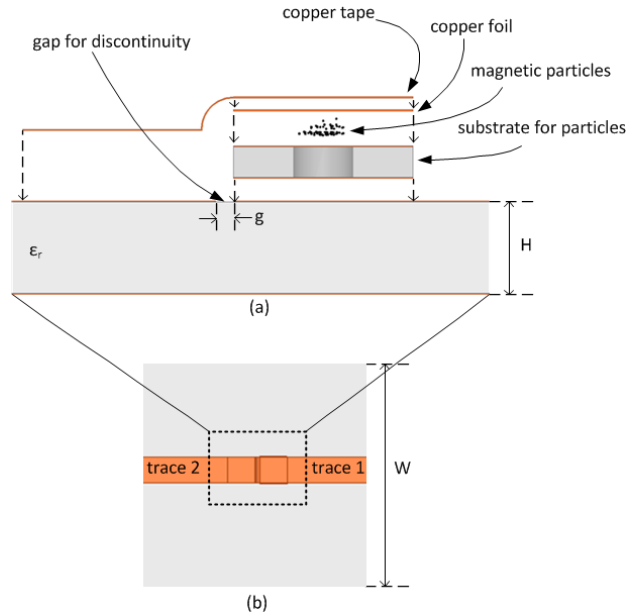
Figure 2.1. Architecture of MRS of (a) Side view segment of MRS and (b) Top view of TL with MRS

8

2.2.1. Simulation Modeling setup for Magnetic Particles

When studying the MRS in the on state, it is unknown how many of the magnetic particles are actually stacking, leading to questions regarding simulation setup within HFSS. Following the average diameter of the particles, they were modeled in HFSS while stacked together to form columns. According to [25], the number of columns stacked in HFSS makes little to no difference between the simulation comparisons. So this work assumes a total of five columns of magnetic particles stacking to turn the MRS on. This setup can be seen in Fig. 2.2 and has shown promising comparisons with measurements, which will be discussed in the next session. The meshing of the magnetic particles can be seen in Fig. 2.3, showing sufficient mesh sizes to handle this simulation accurately.
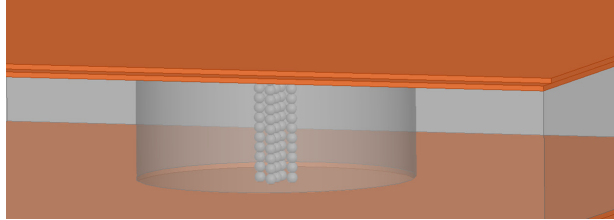
Figure 2.2. Magnetic particle setup for HFSS simulation
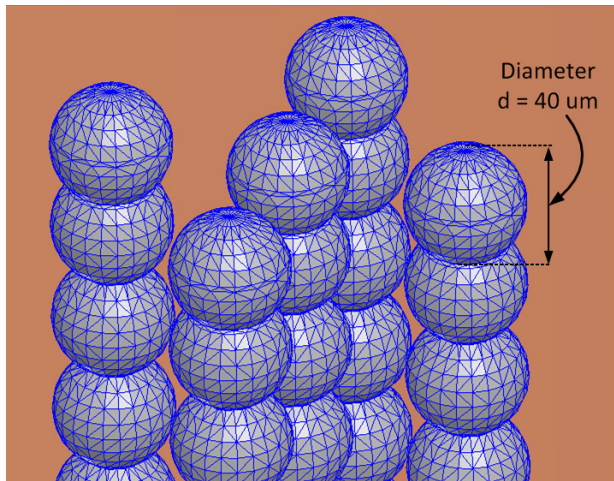
Figure 2.3. HFSS simulation mesh for magnetic particles

9
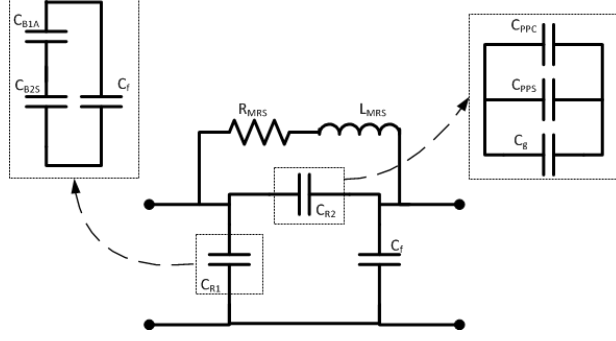
Figure 2.4. Equivalent circuit of MRS. $C_{R1} = 0.053253$ pF, $C_{R2} = 0.711215$ pF, $C_f = 0.011$ pF, $C_{B1A} = 0.05166$ pF, $C_{B2S} = 0.23205$ pF, $C_f = 0.011$ pF, $C_{PPC} = 0.013015$ pF, $C_{PPS} = 0.6118$ pF, $C_g = 0.0864$ pF, $L_{MRS} = 0.77368$ nH, $R_{MRS} = 1$ $\mu\Omega$ (on) and 100 $k\Omega$ (off)

2.3. Extracted Equivalent Circuit of the Component

An equivalent circuit that models the MRS is illustrated in Fig. 2.4. C_{R1} consists of C_{B1A} and C_{B2S} in parallel with C_f where C_{B1A} and C_{B2S} are the parallel plate capacitances between the tape and ground plane over the gap through the air and TMM4 boundaries, respectively, and are calculated using the well known equation for capacitance

$$C = \frac{\epsilon_r \epsilon_o A}{h} \tag{2.1}$$

where A is the cross sectional area, ϵ_o is the permittivity of free space and h is the distance between the plates in meters. C_f is the fringing capacitance caused by the non terminated end of the TL found using the following equations [27]:

$$C_f = \frac{1}{2}C_e \tag{2.2}$$

where

$$\frac{C_e}{t_w}(pF/m) = 12\left(\frac{\epsilon_r}{9.6}\right)^{0.9}\left(\frac{g}{t_w}\right)^{m_e}exp(t_e), \tag{2.3}$$

$$m_e = 0.8675 \tag{2.4}$$

and

$$t_e = 2.043\left(\frac{t_w}{H}\right)^{0.12}. \tag{2.5}$$

10

The variable t_w is the 50 Ω trace width, C_{R2} is made up of components C_{PPC}, C_{PPS}, and C_g in parallel, where C_{PPC} and C_{PPS} are the parallel plate capacitances through the air and substrate, respectively, between the top and bottom of the MRS, calculated using (2.1). C_f is a second fringing capacitance on trace 2 found similarly to C_f while C_g is the gap capacitance caused from the gap between the noncontinuous TLs found from [27] using the equations

$$C_g = \frac{1}{2}C_o - \frac{1}{4}C_e \tag{2.6}$$

where

$$\frac{C_o}{t_w}\,(pF/m) = \left(\frac{\epsilon_r}{9.6}\right)^{0.8}\left(\frac{g}{t_w}\right)^{m_o} exp\,(t_o), \tag{2.7}$$

$$m_o = \frac{t_w}{H}\left[0.619\,log\left(\frac{t_w}{H}\right) - 0.3853\right] \tag{2.8}$$

and

$$t_o = 4.26 - 1.453\,log\left(\frac{t_w}{H}\right). \tag{2.9}$$

When in the on state, the magnetic particles stack vertically and can be represented as a standard via with the assumption they are packed tightly together. Therefore, the L_{MRS} can be modeled as the inductance of the via, and was found using the equation [28]:

$$L_{MRS} = \frac{\mu_o}{2\pi}\left[h\,ln\left(\frac{h + \sqrt{r^2 + h^2}}{r}\right) + \frac{3}{2}\left(r - \sqrt{r^2 + h^2}\right)\right] \tag{2.10}$$

where r is the radius of the magnetic particles. The average amount of particles per MRS is approximately 1000, found from using a small measuring cup and manually counting the number of particles within it under a microscope. Then, assuming an average particle diameter of 20 μm and all particles are tightly packed, the radius of the via can be calculated to be about 128 μm. Finally, R_{MRS} is set as a low impedance (1 $\mu\Omega$) when the MRS is in the on state and a high impedance (100 $k\Omega$) when in the off state.

Fabricated MRSs as well as simulated RLC boundaries and structures within HFSS may be viewed in Fig. 2.5. The manufactured MRS is shown in Fig. 2.5 (a) next to the HFSS simulated MRS 3D model and RLC model in Figs. 2.5 (b) and (c), respectively. Notice in Fig. 2.5 (c) that the HFSS lumped component does not consist of the entire equivalent circuit shown in Fig. 2.4. This

11
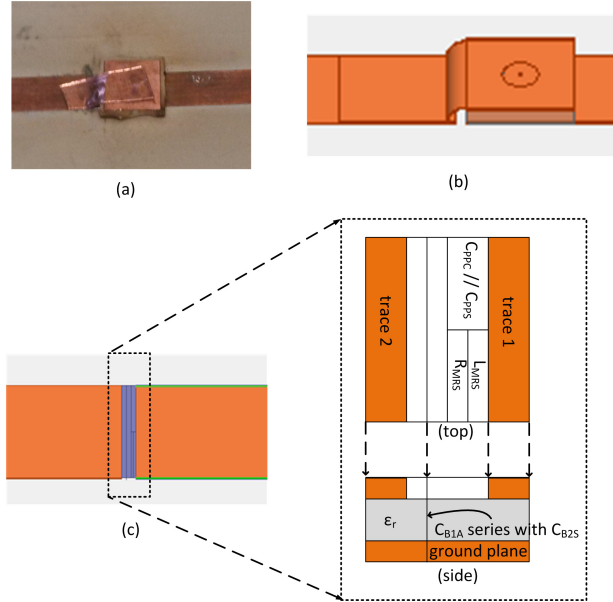
Figure 2.5. Modeling of MRS for (a) Fabricated (b) HFSS structure (c) HFSS RLC boundaries

is due to the HFSS structure still consisting of two transmission lines, therefore, the two fringing capacitances (C_f) and gap capacitance (C_g) are already taken into account.

The equivalent circuit can be more easily understood by viewing Fig. 2.6 where component positions can be seen inside of the 3D model. S-parameters of the measured vs simulated are shown in Fig. 2.7 and Fig. 2.8, where you can see very similar results between the lumped RLC simulation, FEM simulation and measurements verifying the accuracy of the equivalent circuit. In Fig. 2.7 you can see the MRS has an effective Reflection coefficient (under 10 dB) past 3.0 GHz. In Fig. 2.8, it can be seen that the MRS functions well (under 10 dB) as an RF switch in the off state up to about 300 MHz. At this point, $|S_{12}|$ is being weakened due to the capacitive coupling of the MRS, caused primarily by the cross sectional area of the MRS.
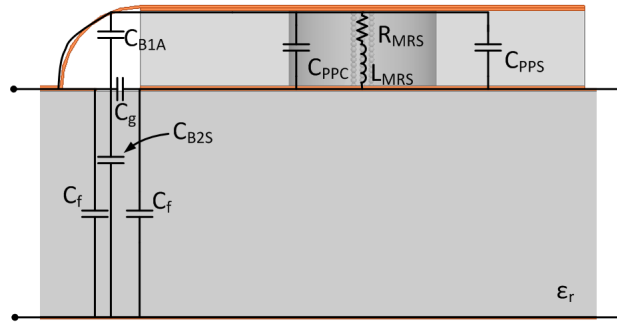
Figure 2.6. Side view of the equivalent circuit within the 3D model

12
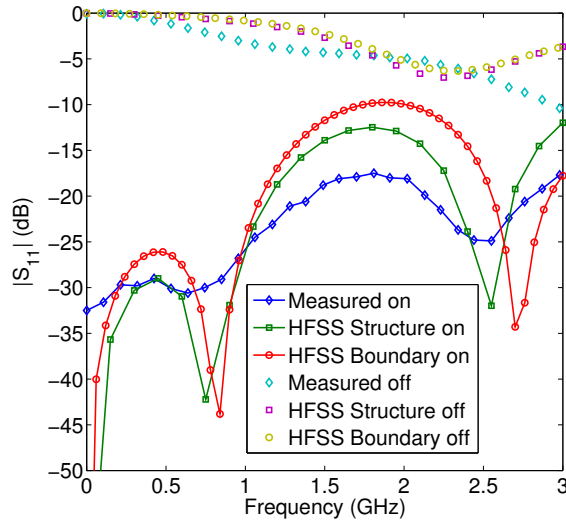
Figure 2.7. $|S_{11}|$ for MRS, $|S_{22}|$ is similar to $|S_{11}|$
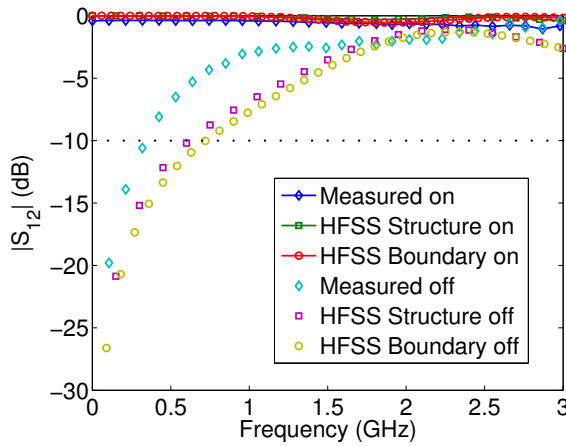
Figure 2.8. $|S_{12}|$ for MRS, $|S_{21}|$ is similar to $|S_{12}|$

2.3.1. Comparison to Previous Circuit

This circuit is proposed as an advancement to the previous circuit given in [25]. Previously, the equivalent circuit was modeled in Advanced Design System (ADS) with a 3D structural model being simulated in HFSS. In the proposed work, the same model will be simulated in HFSS, but the equivalent circuit will use the new proposed circuit, and it will be simulated using the HFSS RLC lumped boundaries in HFSS. Both the work proposed in this paper and the work proposed in [25],

13
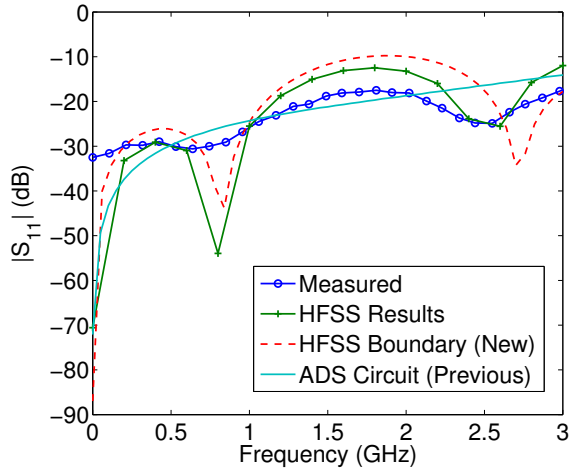
Figure 2.9. $|S_{11}|$ for the MRS in the on state, circuit from [25] compared to new circuit, $|S_{22}|$ is similar to $|S_{11}|$

have presented the same measured results, as well as the same HFSS model results. However, the previous and current results using the lumped components have differences. It can be seen in Fig. 2.9 that the HFSS lumped RLC boundary and 3D model match very well in the on state. While at first glance the previous circuit appears to match the measured results better, it should be noted that the previous circuit lacks the well defined $|S_{11}|$ dips that the measured results display, while the new circuit displays similar dips. In Fig. 2.10, similar results can be seen between the previous circuit and the new circuit, however, the new circuit lies closer to measured results.
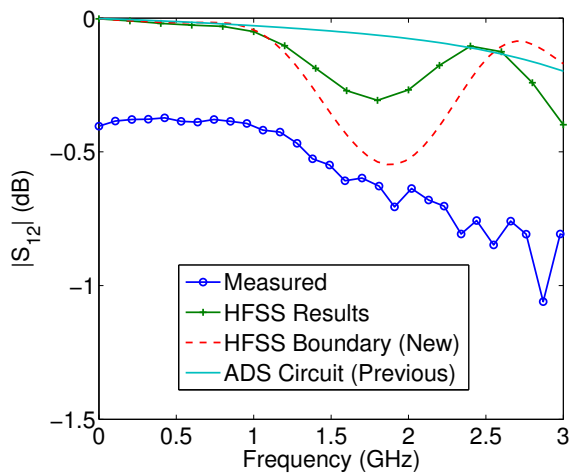
Figure 2.10. $|S_{12}|$ for the MRS in the on state, circuit from [25] compared to new circuit, $|S_{21}|$ is similar to $|S_{12}|$

14
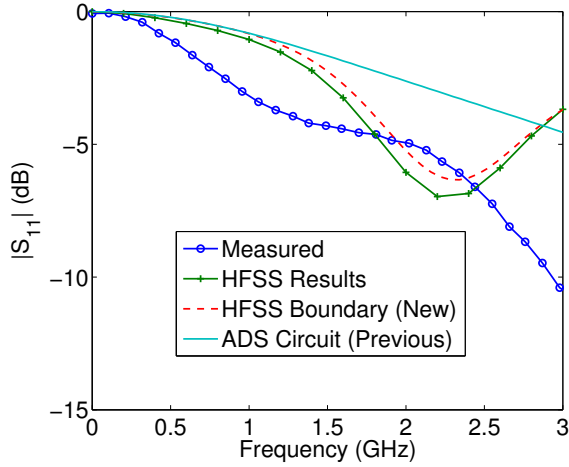
Figure 2.11. $|S_{11}|$ for the MRS in the off state, circuit from [25] compared to new circuit, $|S_{22}|$ is similar to $|S_{11}|$

In the off state, it can be seen in Fig. 2.11 that the HFSS model and HFSS lumped boundary match closely together, as well as near to the measured results while the previous circuit presented in [25] is over 5 dB too high. Finally, it can be seen in Fig. 2.12 that both the previous circuit, new circuit, and HFSS model are very close together, not far from the measured results. Even so, the previous circuit still is furthest away from the measured results, leading to the conclusion that the new circuit is more accurate than the circuit presented in [25].
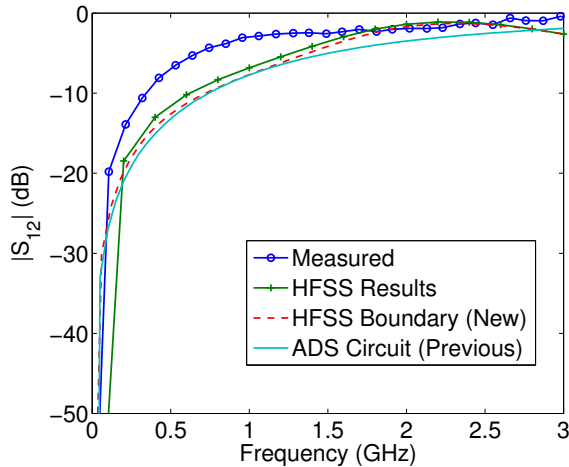
Figure 2.12. $|S_{12}|$ for the MRS in the off state, circuit from [25] compared to new circuit, $|S_{21}|$ is similar to $|S_{12}|$

15

2.4. Conclusions

The equivalent circuit theory was studied of a new magneto-static responsive structure (MRS). Initially, an equivalent circuit was proposed of the new MRS and results were compared to two separate HFSS simulations, the first using a standard modeling procedure and the second using lumped RLC boundaries. Results showed a good comparison between the equivalent circuit simulations and measurements, and that the switch has a good reflection coefficient past 3.0 GHz and a sufficient $|S_{12}|$ up to 300 MHz. Then, the proposed circuit was compared with the previous circuit proposed in [25]. Results show the new circuit is more accurate, displaying appropriate harmonics and similar values to that of the measured. Differences between measured results and simulations are likely due to extra losses when taking measurements.

3. RINGING AND OVERSHOOT CHARACTERISTICS OF THE MAGNETO-STATIC RESPONSIVE STRUCTURE

3.1. Introduction

Signal integrity (SI) is a very important topic in the modern world of high frequency design and electromagnetic compatibility. Without proper practices when designing systems, SI can be compromised effecting the system's computing time, power, and ability to process the information correctly. One important area within SI, is the overshoot and ringing of a digital square wave. Naturally, there is no perfect square wave, each square wave has its own overshoot and ringing characteristics caused by electrical noise, impedance mismatch, bandwidth of the interconnect, and other factors. These characteristics can make deciphering electrical data more difficult not only due to the need for picking out the correct signal, but more cumbersome to any system, whether it is an integrated circuit, printed circuit board, or the inter-system connections[29] that have ever increasing problems caused from increasing clock speeds and shorter rise times [30, 31]. This especially becomes a problem with wireless communications which require long distance deciphering of data, motivating work for developing technology revolving around the SI characteristics of a radio frequency (RF) signal. SI characteristics of the magneto-static responsive structure (MRS) have been studied and will be presented in the following sections.

3.2. Test Procedure

The MRS setup was constructed as shown in Fig. 2.1 and the Pin diode setup was constructed similarly just by replacing the MRS with a Pin diode (part number SMP1322-079LF) and adding a pair of RF chokes (part number ADCH-80A), A continuous TL board was constructed with no gap for discontinuity to be compared to both the MRS and Pin diode setups and is shown in Fig. 3.1 (a). The MRS and Pin diode boards are shown in Fig.3.1 (b) and Fig. 3.1 (c), respectively. Two of each type of board was manufactured, then all six boards were consecutively connected to a function generator and an oscilloscope to be tested at 10.0 MHz and 40.0 MHz. A 0 dBm, -0.5 to 0.5 volt square wave was sent from a function generator to the oscilloscope through separate cables and the device under test, as shown in Fig.3.2 (a)-(c). Then the measured square wave in the
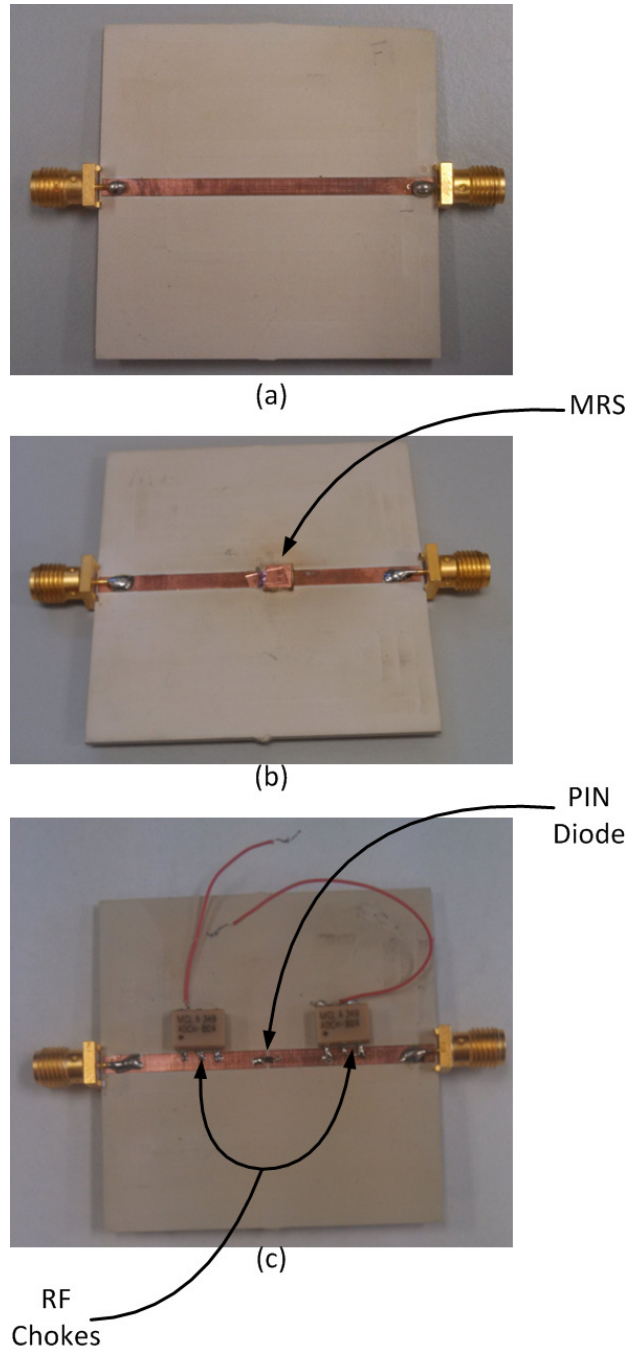
Figure 3.1. Manufactured prototypes of test setups with (a) Continuous TL and (b) MRS TL and (c) Pin diode TL

oscilloscope was extracted and averaged with the same board of that setup. The average of each setup was plotted in MATLAB for comparison. Small permanent magnets were used in activating the MRS. By introducing the magnets the TL would function in the on state. By removing the magnets, the TL would function in the off state. For the Pin diode configuration, a 0.7 volt DC
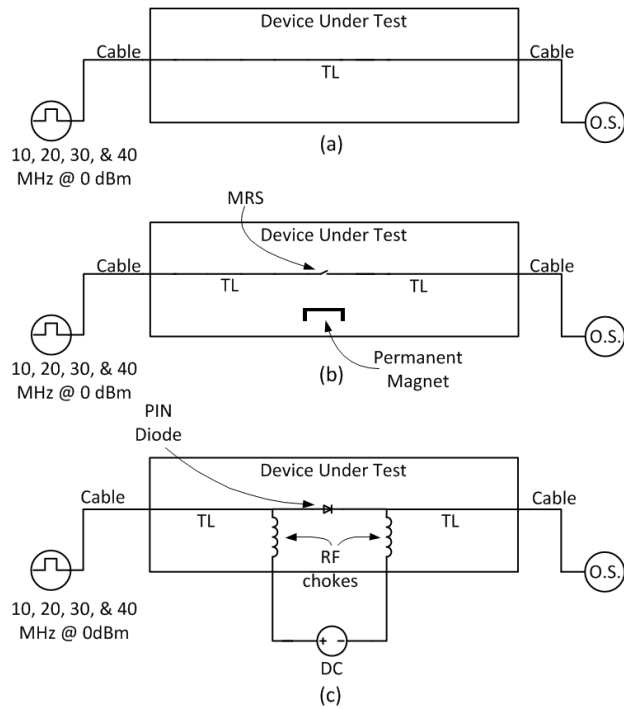
Figure 3.2. Measurement setup of the test procedure for (a) Continuous TL (b) MRS and (c) Pin diode

bias was used to activate it. In doing so, the square wave measured also had an offset of 0.7 volts. To correct this, the data extracted was shifted that same 0.7 volts for comparisons.

3.3. Results and Discussions

The plots of the overshoot and ringing at 10.0, 20.0, 30.0, and 40.0 MHz can be seen in Figs. 3.3, 3.4, 3.5, and 3.6, respectively. It is shown that while the MRS configuration has very similar characteristics to the continuous TL, the Pin diode is a bit more lossy, where this lossy nature of the Pin diodes will effect PCBs and interconnects in a negative manner. Intuitively, these
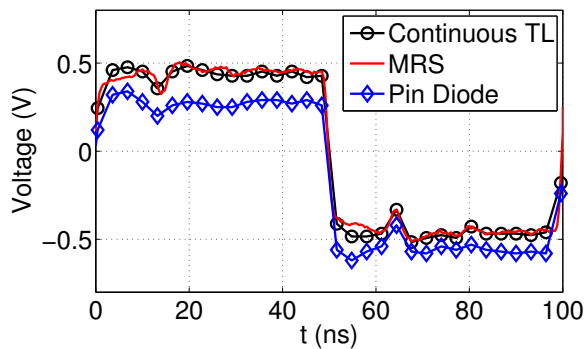
Figure 3.3. Ringing and overshoot measurement comparisons at 10 MHz
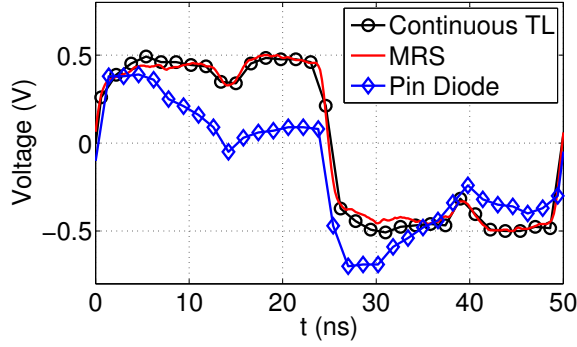
Figure 3.4. Ringing and overshoot measurement comparisons at 20 MHz

additional losses make sense due to the extra DC voltage and RF chokes required with the Pin diode configuration, which all cause additional electrical noise. Whereas the MRS is more similar to a wire connection when turned on. Next, the 10-90 bandwidth (BW) of the three setups was calculated using the formula [30]:

$$BW = \frac{0.35}{R_t} \tag{3.1}$$

where R_t is the 10-90 rise time of the square wave. These results can be seen in Table 3.1, where it is shown that the 10-90 BW for these setups are all well over 80 MHz, which is a minimum desired. Take note at the 20.0 MHz BW for the Pin diode, the BW appears to be quite large, although this is actually caused by the losses for the diode. Also it should be noticed that all of the square waves have an average of about 0 volts, as expected, except for the Pin diode at 20.0 MHz, which appears to have an average of -0.2 volts. It is the author's belief that this is due to a unique resonance of the Pin diode at 20.0 MHz, which would also explain the extra losses at this frequency.

Average comparisons of the BW between the continuous TL, MRS, and Pin diode were
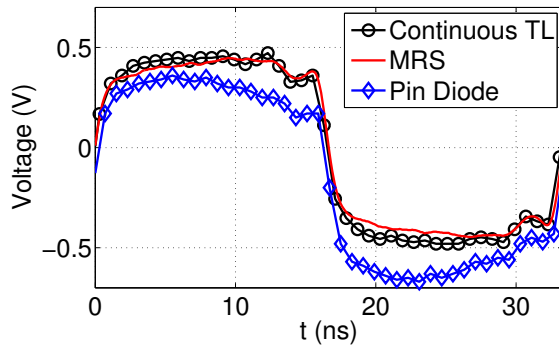
Figure 3.5. Ringing and overshoot measurement comparisons at 30 MHz

20
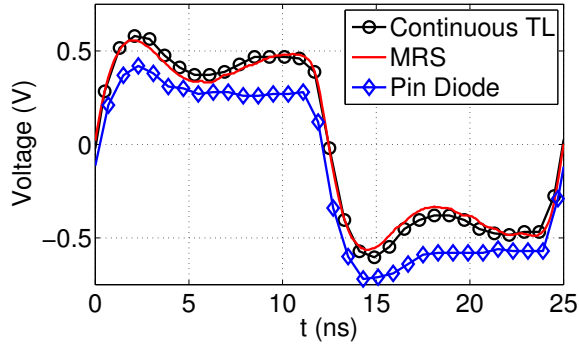
Figure 3.6. Ringing and overshoot measurement comparisons at 40 MHz

Table 3.1. Bandwidth measurements of the continuous TL, MRS, and Pin diode configurations, all units in MHz

Bandwidth	Continuous TL	MRS	Pin diode
@10.0 MHz	179.211	197.072	222.363
@20.0 MHz	163.551	162.112	451.031
@30.0 MHz	125.899	147.306	161.290
@40.0 MHz	232.558	186.071	245.442

calculated between the four frequencies used. On average, the BW of the MRS was within 88.88% to the BW of the continuous TL, while the BW of the Pin diode was within 72.93% to the BW of the TL. Showing that on average, the MRS is almost 16% more similar to the continuous TL then the Pin diode in regards to bandwidth. Prior to this research, MEMS would be used to address the lossy nature of the Pin diode. However, MEMS introduce the problem of moving parts and high activation voltages. With the MRS, the lossy nature of Pin diodes can be avoided, as well as the moving parts and high activation voltages that would be required with MEMS.

3.4. Conclusions

The MRS overshoot and ringing characteristics were measured and compared with those of a continuous TL and Pin diode configuration. These results showed similar characteristics between the continuous TL and MRS configurations, however, extra losses were seen within the Pin diode configuration, likely due to additional components such as the RF chokes or the diode parasitics. Overall though, the MRS has shown promise in its use as an RF switch due to the minimum ringing and overshoot associated with it. Unlike the Pin diode, the MRS maintains a good square wave which is useful for a PCB or interconnect that requires deciphering digital data.

4. A VARIABLE EFFECTIVE PERMITTIVITY STRUCTURE CONSISTING OF THE MAGNETO-STATIC RESPONSIVE STRUCTURES

4.1. Introduction

The variable effective permittivity structure (VEPS) is composed of several magneto-static responsive structures (MRS) built into a substrate, where a portion of the VEPS can be seen in Fig. 4.1. The VEPS is meant to operate similarly to the well known mushroom structure described in Chapter 1. However, earlier mushroom structures all share similar shortcomings. With the via in place, they all operate in a fixed manner. This work replaces the via's with conductive magnetic particles as presented earlier. In this manner, we have the ability to activate and deactivate the mushroom structures with the introduction of a magnetic field.
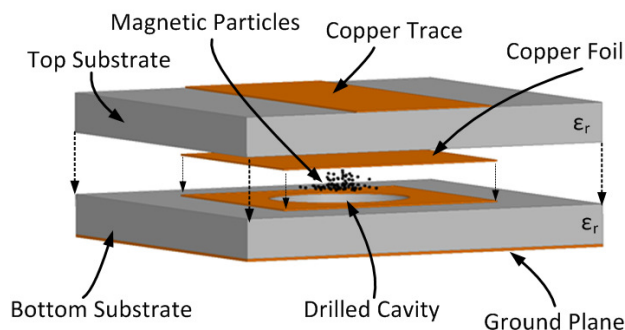
Figure 4.1. Architecture of a portion of the proposed variable effective permittivity structure (VEPS)

4.2. Architecture of Structure

The architecture of the VEPS consists of two separate substrates stacked on top of each other. The top substrate shown in Fig. 4.2 consists of a single copper clad (cu) board of Rogers TMM4 material ($\epsilon_r = 4.5$) with a height $H_v = 0.508$ mm and width W $= 50$ mm. Then a 50 Ω trace ($t_w = 1.9$ mm) is milled out of the top plane. The bottom substrate shown in Fig. 4.3 consists of a double copper clad board of Rogers TMM4, also with a height H_v and width W. For this substrate, 3 x 3 mm (w x w) copper patches are milled out of the top plane down the center of the substrate
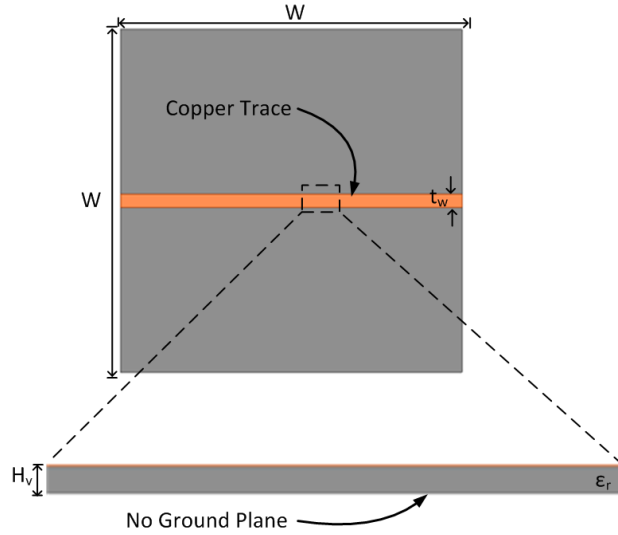
Figure 4.2. Top layer of the variable ϵ_{reff} structure with top view (above) and expanded side view (below)
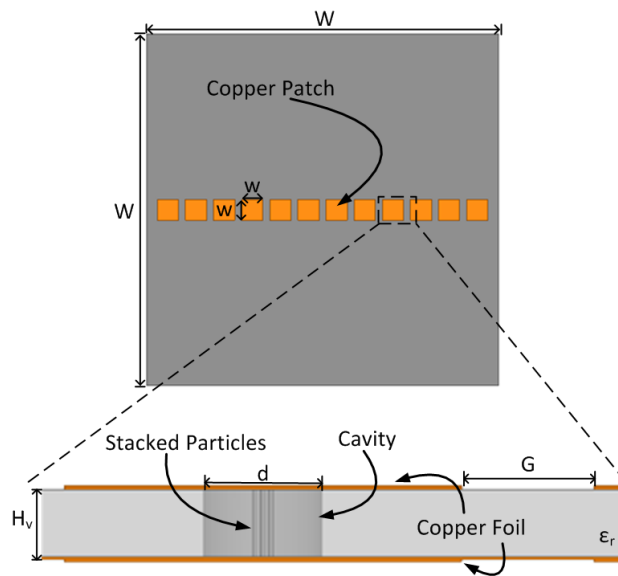
Figure 4.3. Bottom layer of the Variable ϵ_{reff} structure with top view (above) and expanded side view (below)

with a gap G = 1 mm separating each patch. A cavity d = 0.9 mm is drilled out of the center of these patches through the ground plane. Then, copper foil is secured on the ground plane as described in Chapter 2. Followed by filling the cavities with the conductive magnetic particles also described in Chapter 2. Then copper foil is secured on the copper patch above the cavity. Finally, the top and bottom substrates are stacked shown in Fig. 4.4 to form one structure that can be seen in Fig. 4.5.
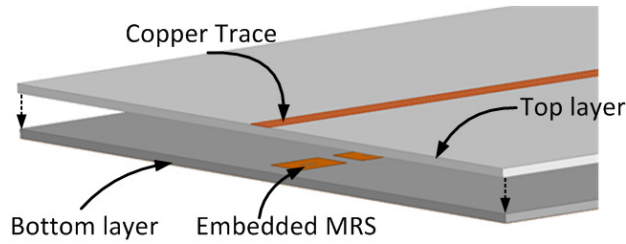
Figure 4.4. Expanded view of the variable ϵ_{reff} structure
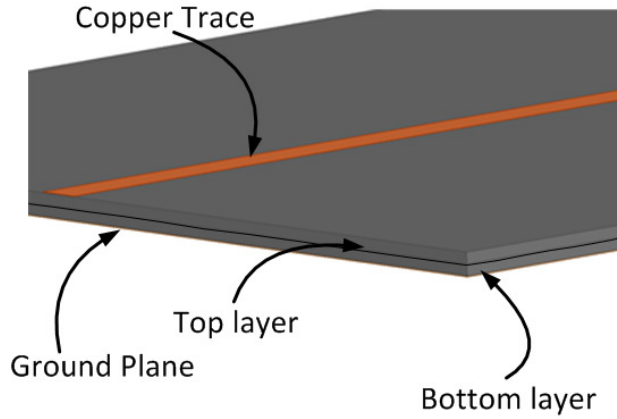
Figure 4.5. Assembled variable ϵ_{reff} structure

4.3. HFSS Simulations

4.3.1. Simulation Setup

Originally, the same simulation setup from Chapter 2 was going to be used for this work as well. However, when implementing such a large amount of the MRSs composing of spherical columns into the simulation, the required time and RAM was too high to be effective when running the simulations, motivating an effort to find a less strenuous modeling structure. The structure shown in Fig. 4.6 was proposed, where instead of overlapping spherical particles, the assumption is
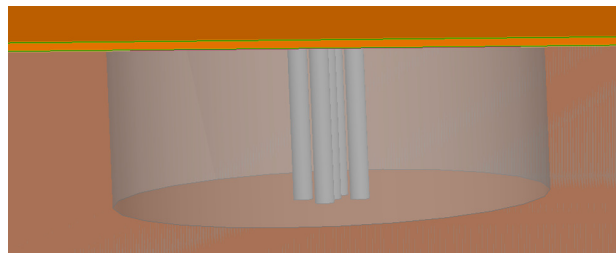
Figure 4.6. View of uniform cylinders that replace the original overlapping spheres for simulation
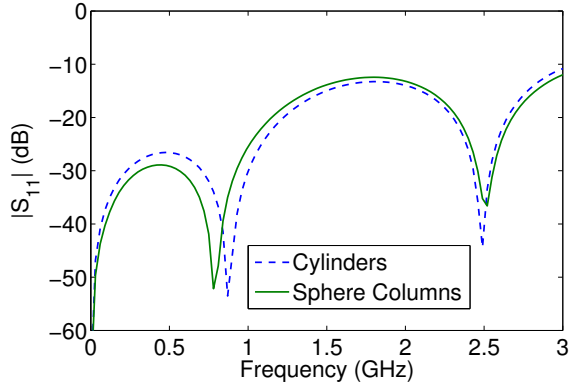
Figure 4.7. $|S_{11}|$ comparison between the cylinder columns and the spherical columns

made that a uniform cylinder of equal diameter d = 40 um will have similar results in simulations. It can be seen in Figs. 4.7 and 4.8 that the S-parameter comparisons between the spherical columns and the cylinders are similar for this application, so for the following simulations the cylinders will be used to save on computational time and power. Using the geometry as shown in Fig. 4.5, several VEPSs were modeled and simulated in the computer simulation program HFSS. In Fig. 4.3, it can be seen that twelve MRSs are embedded within the VEPS. We ran simulations for this structure, as well as structures consisting of 1, 2, 4, 6, 8, and 10 MRSs embedded into each. Results were then tabulated and plotted against each other for comparison.

4.3.2. Simulated S-Parameter Results of the Variable Effective Permittivity Structure

$|S_{11}|$ and $|S_{12}|$ parameters for the VEPS with variable amounts of MRS embodiments in the off state can be seen in Figs. 4.9 and 4.10, respectively. From Fig. 4.9, it can be noted that all of the VEPSs operate well (under 10 dB) past 5 GHz. A closer look at Fig. 4.9 presents
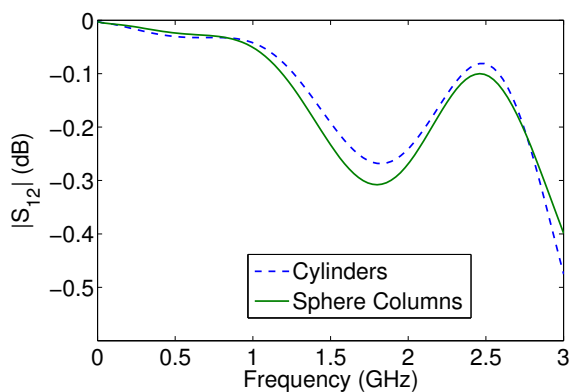
Figure 4.8. $|S_{12}|$ comparison between the cylinder columns and the spherical columns

25
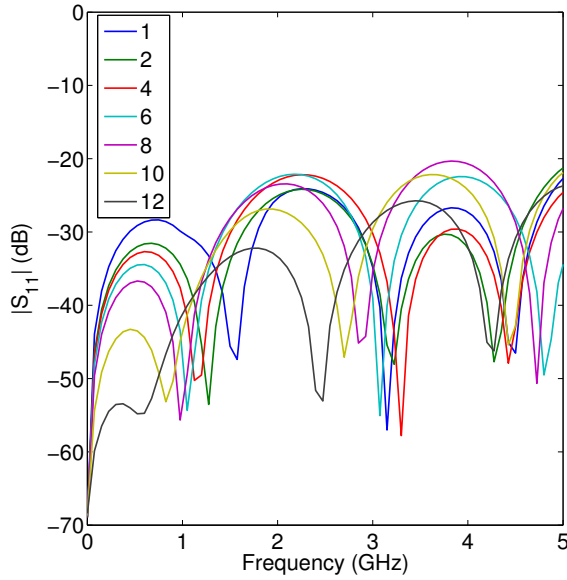
Figure 4.9. $|S_{11}|$ for the VEPS with variable amounts of MRSs in the off state in HFSS, $|S_{22}|$ is similar to $|S_{11}|$

that the larger amount of embedded MRSs that are within the structure, the better the structure operates up to about 3 GHz. From Fig. 4.10, it can be summarized that the VEPS has a good $|S_{12}|$ parameter (above -3 dB) past 5 GHz as well. This information can be summarized as stating in the off state that the VEPS operates well as a trace past 5 GHz.

$|S_{11}|$ and $|S_{12}|$ for the VEPS with variable amounts of MRS embodiments in the on state can be seen in Figs. 4.11 and 4.12, respectively. From Fig. 4.11, it can be seen that all of the
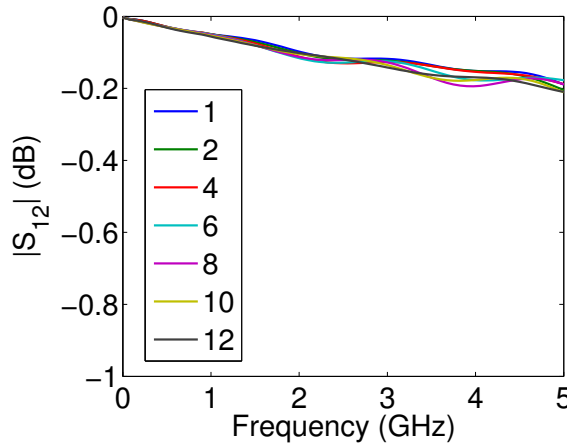
Figure 4.10. $|S_{12}|$ for the VEPS with variable amounts of MRSs in the off state in HFSS, $|S_{21}|$ is similar to $|S_{12}|$

26
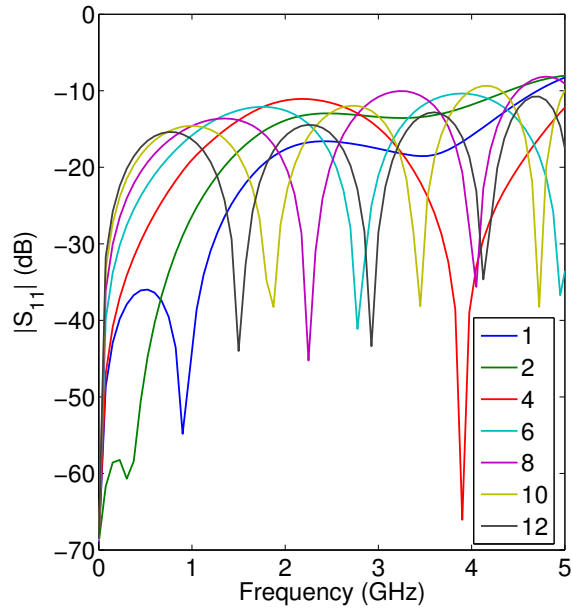
Figure 4.11. $|S_{11}|$ for the VEPS with variable amounts of MRSs in the on state in HFSS, $|S_{22}|$ is similar to $|S_{11}|$

VEPSs operate well (Reflection coefficient under -10 dB) up to about 4 GHz, and just above -10 dB at 5 GHz. The $|S_{12}|$ values can be seen in Fig. 4.12, and here, it should be noted that the larger amount of MRSs embedded, the larger of an effect on the $|S_{12}|$ values.
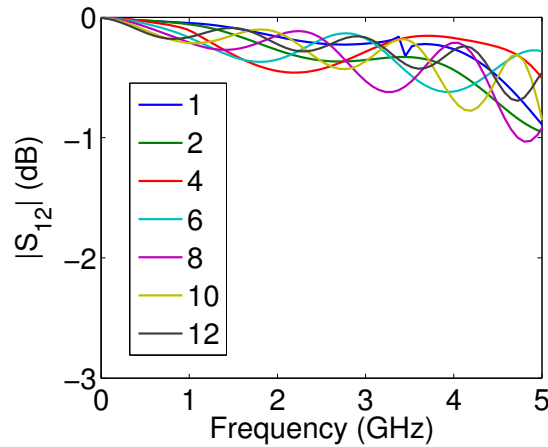
Figure 4.12. $|S_{12}|$ for the VEPS with variable amounts of MRSs in the on state in HFSS, $|S_{21}|$ is similar to $|S_{12}|$

27
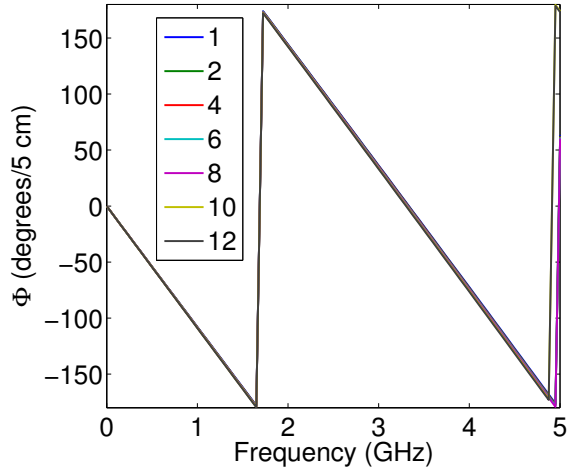
Figure 4.13. Phase diagram for the VEPS with variable amounts of MRSs in the off state in HFSS

4.3.3. Simulated β and ϵ_{reff} Results of the Variable Effective Permittivity Structure

A Phase plot of the VEPS with variable amounts of MRS embodiments in the off state can be seen in Fig. 4.13, where it can be seen that there is little to no change in phase throughout the VEPS with varying amounts of MRSs. To extract β from Fig. 4.13, one can apply the formula

$$\beta = \phi - 360(n) \tag{4.1}$$
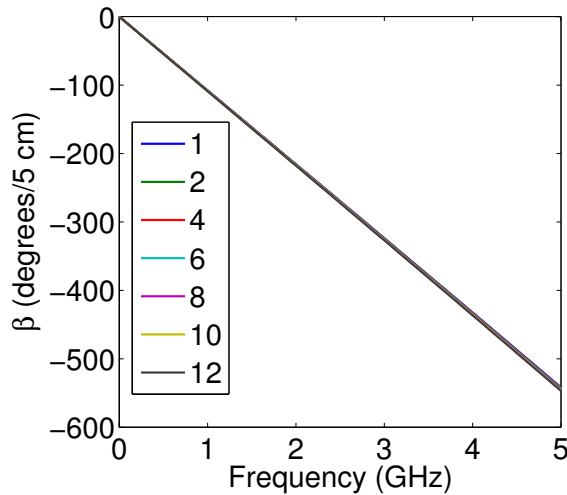
Figure 4.14. β diagram for the VEPS with variable amounts of MRSs in the off state in HFSS

Table 4.1. β of VEPS with varying amounts of embedded MRSs in the off state, all units in degrees/5 cm

Frequency	1 MRS	2 MRSs	4 MRSs	6 MRSs	8 MRSs	10 MRSs	12 MRSs
@1.0 GHz	-107.9	-108	-108.2	-108.35	-108.55	-108.75	-108.95
@2.0 GHz	-215.7	-216.1	-216.3	-216.6	-217	-217.4	-217.8
@3.0 GHz	-323.5	-324.3	-324.5	-325	-325.7	-326.5	-327
@4.0 GHz	-432.5	-433	-433.5	-434	-434.75	-435.75	-436.5
@5.0 GHz	-542	-542.5	-543.25	-543.75	-544.75	-546	-546.75

where ϕ is the phase value at a frequency and n is the number of phase shifts (number of times the phase shifted from -180 to +180) up to that particular frequency. This plot can be seen in Fig. 4.14. It should be noted that there is little to no change in β. A summarized and tabulated view of these results can be seen in Table 4.1, where it can be gathered that in the off state, there is only a few degrees of difference between the different VEPSs, a maximum difference of 14 degrees can be observed between a VEPS with one embedded MRS and a VEPS with 12 embedded MRSs at 5 GHz, which is a very minimal difference, showing that all of the VEPSs have very similar β characteristics in the off state. Finally, to extract the ϵ_{reff}, the formula

$$\epsilon_{reff} = \frac{\beta}{k_o} \tag{4.2}$$

from [32] was used, where k_o is the free space propagation constant

$$k_o = \frac{\omega}{c_o} \tag{4.3}$$

and c_o is the speed of light in m/s. These formulas were applied when plotting the ϵ_{reff} in the off state, as shown in Fig. 4.15 where it can be seen that all of the VEPS with varying amounts of embedded MRSs have a very similar ϵ_{reff}, this can also be seen in Table 4.2 which summarizes Fig. 4.15. A widely used online ϵ_{reff} calculator from [33] was used for comparison to these results and is shown in Fig. 4.16. Note that the thickness of the dielectric was 1.016 mm due to the top and bottom substrates being stacked, each with a dielectric thickness of 0.508 mm. In Fig. 4.16 you can see the calculated ϵ_{reff} is 3.393. This value lies just above the lines plotted in Fig. 4.15 and the values summarized in Table 4.2, verifying the accuracy of the simulations and calculations. Similarly, all of this work was repeated for the VEPS with varying amounts of MRSs in the on
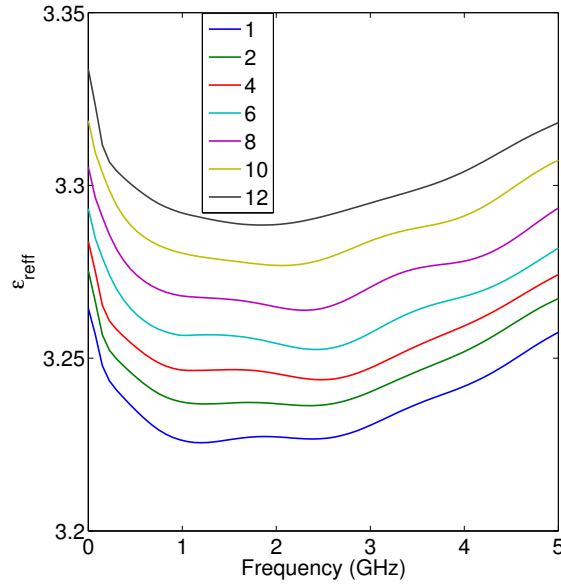
Figure 4.15. ϵ_{reff} of the VEPS with varying amounts of MRSs in the off state in HFSS
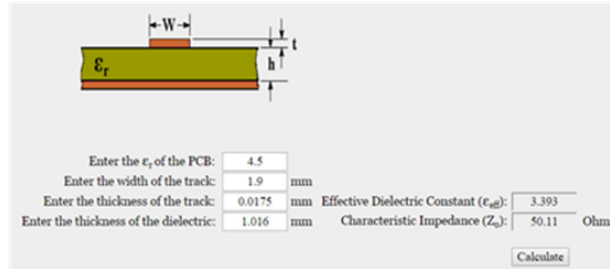
Figure 4.16. Screen capture of the ϵ_{reff} calculator from [33]

state. In Fig. 4.17, you can see the Phase diagram for the VEPS in the on state. Unlike the results shown in Fig. 4.13, the phase is vastly different between the different VEPSs. A plot of the β from the VEPSs in the on state can be seen in Fig. 4.18 as well as a summary of Fig. 4.18 shown in Table 4.3.

Table 4.2. ϵ_{reff} of VEPS with varying amounts of embedded MRSs in the off state in HFSS

Frequency	1 MRS	2 MRSs	4 MRSs	6 MRSs	8 MRSs	10 MRSs	12 MRSs
@1.0 GHz	3.23	3.24	3.25	3.26	3.27	3.28	3.29
@2.0 GHz	3.23	3.237	3.245	3.255	3.265	3.277	3.287
@3.0 GHz	3.23	3.24	3.246	3.258	3.27	3.284	3.294
@4.0 GHz	3.243	3.251	3.259	3.267	3.278	3.291	3.33
@5.0 GHz	3.257	3.267	3.273	3.282	3.293	3.307	3.318
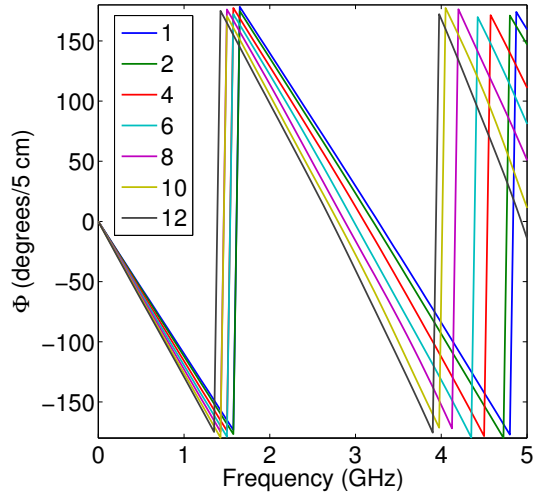
Figure 4.17. Phase diagram for the VEPS with variable amounts of MRSs in the on state in HFSS

Table 4.3. β of VEPS with varying amounts of embedded MRSs in the on state, all units in degrees/5 cm

Frequency	1 MRS	2 MRSs	4 MRSs	6 MRSs	8 MRSs	10 MRSs	12 MRSs
@1.0 GHz	-110	-112	-116	-120	-123	-126	-129
@2.0 GHz	-220	-224	-231	-238	-246	-255	-263
@3.0 GHz	-332	-336	-347	-363	-376	-388	-400
@4.0 GHz	-445	-453	-472	-492	-512	-535	-551
@5.0 GHz	-560	-572	-608	-639	-668	-708	-732

Finally, using the aforementioned formula for finding the ϵ_{reff}, the ϵ_{reff} of the VEPSs in the on state is plotted in Fig. 4.19. A tabular view of these results can also be seen in Table 4.4.
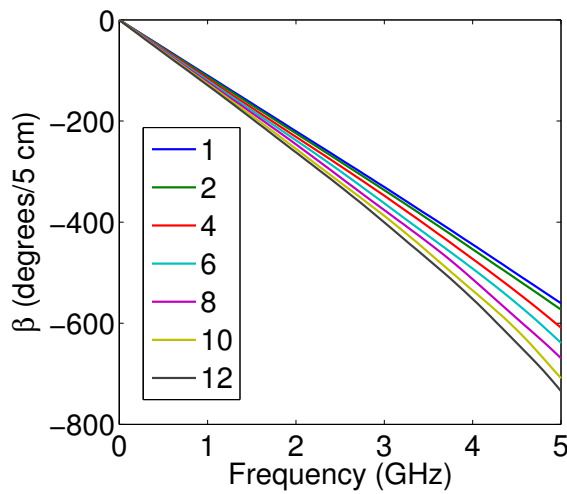
Figure 4.18. β diagram for the VEPS with variable amounts of MRSs in the on state in HFSS

31
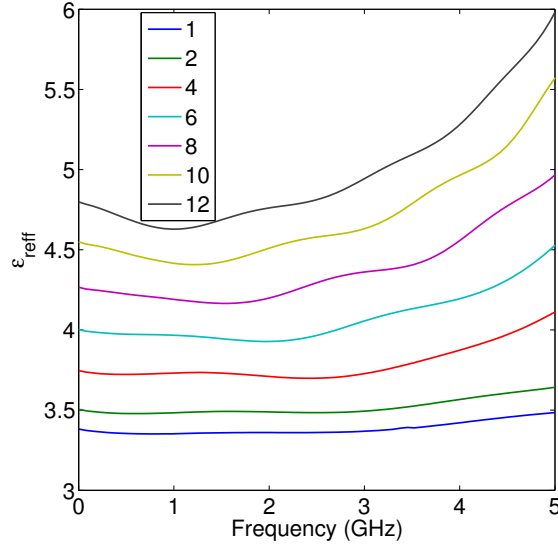
Figure 4.19. ϵ_{reff} of the VEPS with varying amounts of MRSs in the on state in HFSS

Then, finding the difference between Tables 4.1 and 4.3 for the change in β, as well as the difference between Tables 4.2 and 4.4 to find the change in the ϵ_{reff}, gives us Table 4.5 for the change in β and Table 4.6 for the change in the ϵ_{reff}. These results show a large change in the ϵ_{reff}. Tables 4.5 and 4.6 are then plotted into Figs. 4.20, 4.21, and 4.22 for clarity.

Table 4.4. ϵ_{reff} of VEPS with varying amounts of embedded MRSs in the on state in HFSS

Frequency	1 MRS	2 MRSs	4 MRSs	6 MRSs	8 MRSs	10 MRSs	12 MRSs
@1.0 GHz	3.4	3.5	3.7	4	4.2	4.4	4.6
@2.0 GHz	3.4	3.5	3.7	3.9	4.2	4.5	4.7
@3.0 GHz	3.4	3.5	3.7	4.1	4.4	4.6	4.9
@4.0 GHz	3.5	3.6	3.9	4.2	4.6	5	5.3
@5.0 GHz	3.5	3.7	4.2	4.5	5	5.6	6

Table 4.5. Difference in β of the VEPSs with varying amounts of embedded MRSs, all units in degrees/5 cm in HFSS

Frequency	1 MRS	2 MRSs	4 MRSs	6 MRSs	8 MRSs	10 MRSs	12 MRSs
@1.0 GHz	-2.1	-4	-7.8	-11.65	-14.45	-17.25	-20.05
@2.0 GHz	-4.3	-7.9	-14.7	-21.4	-29	-37.6	-45.2
@3.0 GHz	-8.5	-11.7	-22.5	-38	-50.3	-61.5	-73
@4.0 GHz	-12.5	-20	-38.5	-58	-77.25	-99.25	-114.5
@5.0 GHz	-18	-29.5	-64.75	-95.25	-123.25	-162	-185.25

Table 4.6. Difference in the ϵ_{reff} of the VEPSs with varying amounts of embedded MRSs in HFSS

Frequency	1 MRS	2 MRSs	4 MRSs	6 MRSs	8 MRSs	10 MRSs	12 MRSs
@1.0 GHz	0.17	0.26	0.45	0.74	0.93	1.12	1.31
@2.0 GHz	0.17	0.263	0.455	0.645	0.935	1.223	1.413
@3.0 GHz	0.17	0.26	0.454	0.842	1.13	1.316	1.606
@4.0 GHz	0.257	0.349	0.641	0.933	1.322	1.709	1.97
@5.0 GHz	0.243	0.433	0.927	1.218	1.707	2.293	2.682
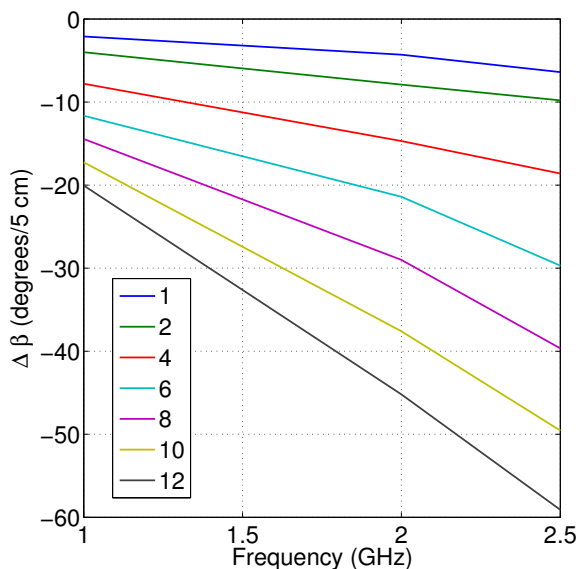
Figure 4.20. Difference of β between the on and off states of the VEPSs up to 2.5 GHz in HFSS

4.4. ADS Simulations

4.4.1. Simulation Setup

The VEPS were modeled in ADS similarly to HFSS next, the primary difference between the simulation setups was that ADS used a solid silver via structure the size of the cavity to represent the VEPS in the on state and a solid air via structure to represent the VEPS in the off state. A screen capture of the ADS 3D viewer can be seen in Fig. 4.23, where the vias representing the stacked particles can be seen through the lower substrate connecting the MRS copper patch to the groudn plane. Board dimensions and simulations are otherwise the same when comparing to HFSS simulations, and again the simulations will be ran with differing amounts of embedded MRSs (1, 2, 4, 6, 8, 10, and 12) within the different VEPSs.

33

Figure 4.21. Difference of β between the on and off states of the VEPSs up to 5 GHz in HFSS
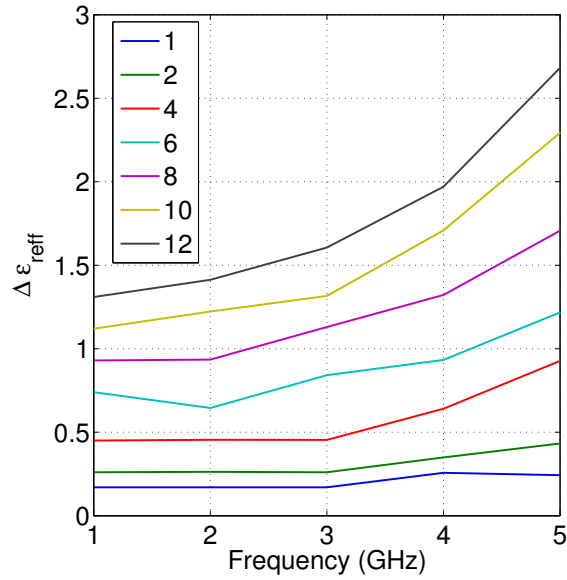
Figure 4.22. Difference of ϵ_{reff} between the on and off states of the VEPSs in HFSS
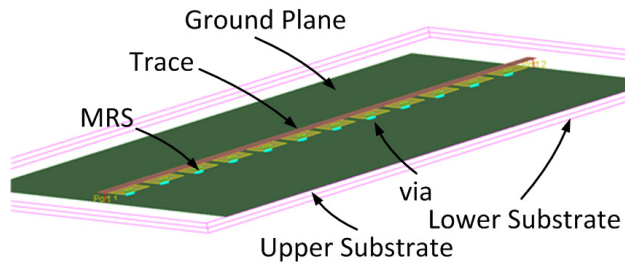
Figure 4.23. Screen capture of the VEPS with 12 embedded MRSs in ADS
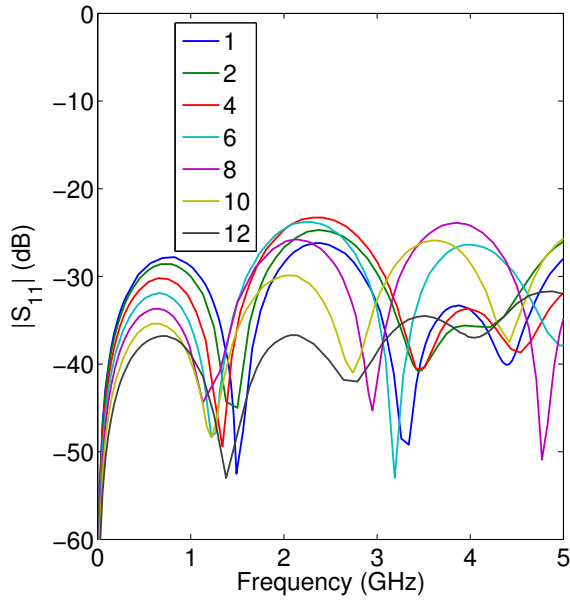
Figure 4.24. $|S_{11}|$ for the VEPS with variable amounts of MRSs in the off state in ADS, $|S_{22}|$ is similar to $|S_{11}|$

4.4.2. Simulated S-parameter Results of the Variable Effective Permittivity Structure

The ADS Simulated $|S_{11}|$ and $|S_{12}|$ values for the VEPS are shown in Figs. 4.24 and 4.25, respectively. These ADS results are similar to the HFSS results shown in Figs. 4.9 and 4.10. In the ADS results, a good reflection coefficient and $|S_{12}|$ can be seen past 5 GHz in the off state. Then after activating the MRSs with a silver via, the $|S_{11}|$ and $|S_{12}|$ values can now be seen in Figs.
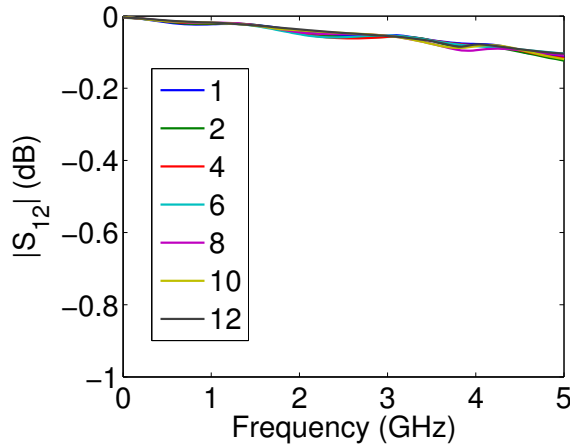
Figure 4.25. $|S_{12}|$ for the VEPS with variable amounts of MRSs in the off state in ADS, $|S_{21}|$ is similar to $|S_{12}|$

35
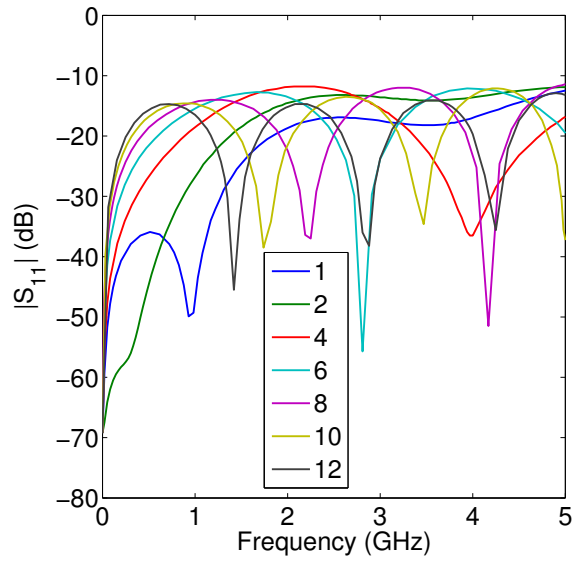
Figure 4.26. $|S_{11}|$ for the VEPS with variable amounts of MRSs in the on state in ADS, $|S_{22}|$ is similar to $|S_{11}|$

4.26 and 4.27. In Fig. 4.26, a match can be seen past 5 GHz, which is similar but a higher value than that of the HFSS result given in Fig. 4.11. Notice that in changing from the off state to the on state that the reflection coefficient increases, this can be expected due to the extra inductance introduced to the substrate by activating the via.
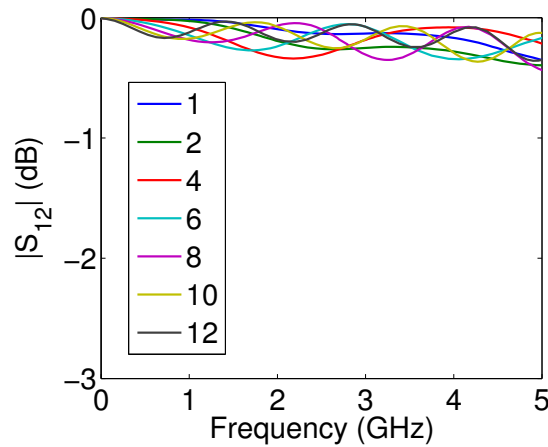
Figure 4.27. $|S_{12}|$ for the VEPS with variable amounts of MRSs in the on state in ADS, $|S_{21}|$ is similar to $|S_{12}|$

36
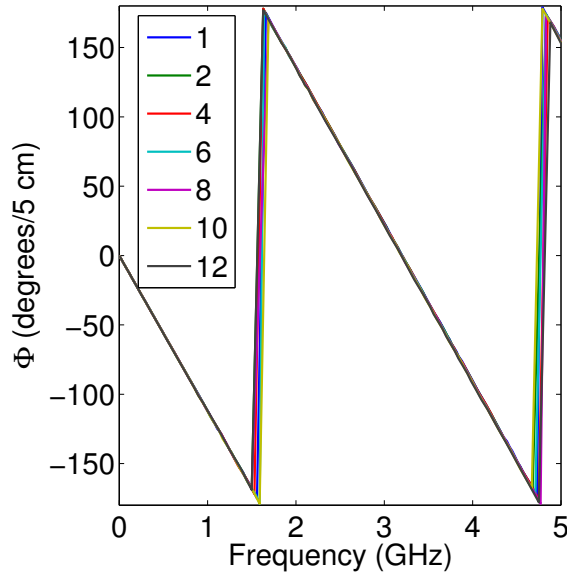
Figure 4.28. Phase diagram for the VEPS with variable amounts of MRSs in the off state in ADS

4.4.3. Simulated β and ϵ_{reff} Results of the Variable Effective Permittivity Structure

Next, a phase plot of the VEPS in the off state for the ADS can be seen in Fig. 4.28, followed by β and ϵ_{reff} plots shown in Figs. 4.29 and 4.30, respectively. As shown with the HFSS plots, there is little to no change in the phase (ϕ), β, or ϵ_{reff} when the VEPSs are in the off state. Also a good match to the online calculated ϵ_{reff} can be seen when comparing Fig. 4.30 to Fig.
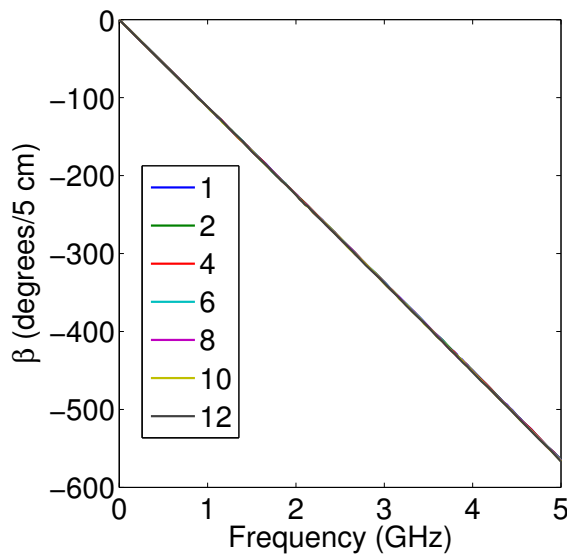
Figure 4.29. β diagram for the VEPS with variable amounts of MRSs in the off state in ADS

37
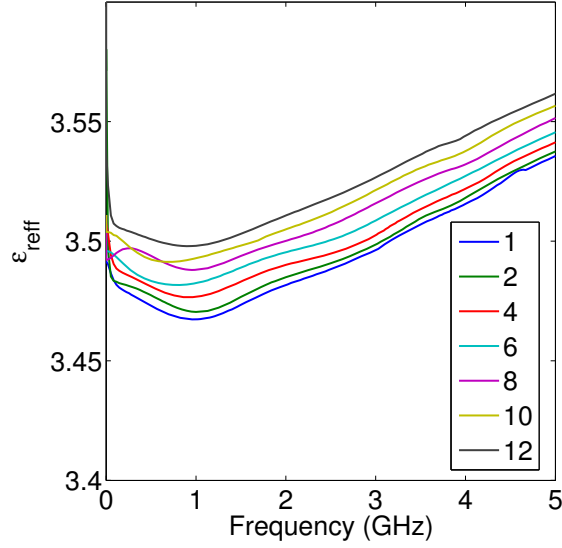
Figure 4.30. ϵ_{reff} of the VEPS with varying amounts of MRSs in the off state in ADS

4.16. However, when the VEPSs are activated through the use of the MRSs, a large difference can be seen in ϕ, β, and ϵ_{reff}, as shown in Figs. 4.31, 4.32, and 4.33. Finally, finding the difference between the on and off states of the ADS simulated VEPSs gives Figs. 4.34, 4.35, and 4.36, where Fig. 4.34 is the difference in β up to 2.5 GHz, Fig. 4.35 is the difference in β up to 5 GHz, and Fig. 4.36 is the change in the ϵ_{reff}. It should be noted how well the HFSS Figs. 4.20, 4.21, and 4.22 match Figs. 4.34, 4.35, and 4.36. These similar results show promise in the manufactured VEPS's
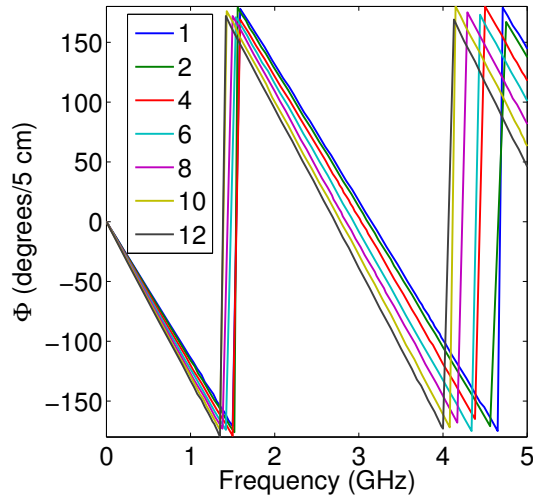
Figure 4.31. Phase diagram for the VEPS with variable amounts of MRSs in the on state in ADS

38
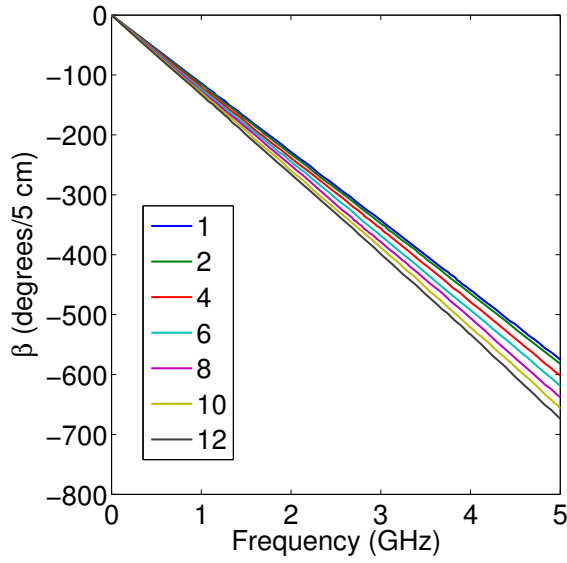
Figure 4.32. β diagram for the VEPS with variable amounts of MRSs in the on state in ADS
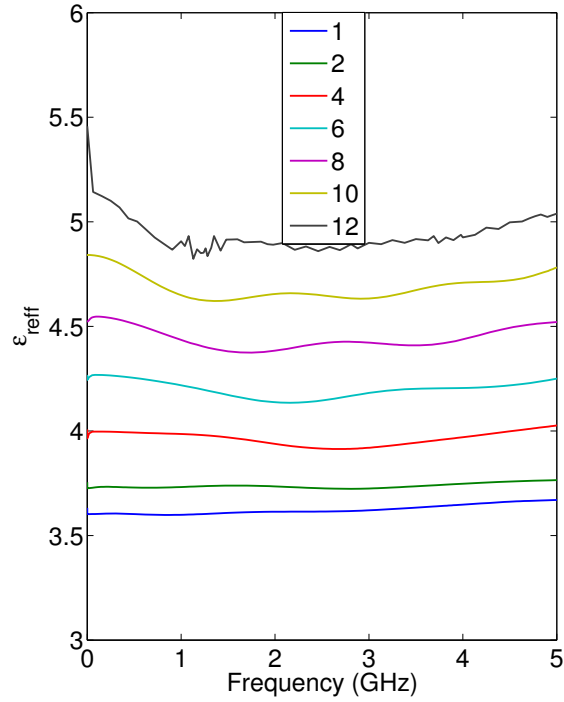
Figure 4.33. ϵ_{reff} of the VEPS with varying amounts of MRSs in the on state in ADS

ability to adjust the phase constant and effective permittivity. These tables and figures provide an excellent baseline for designing a VEPS with the intent of adjusting either the phase constant β or the effective permittivity ϵ_{reff}. It can be seen that by increasing the amount of MRSs embedded
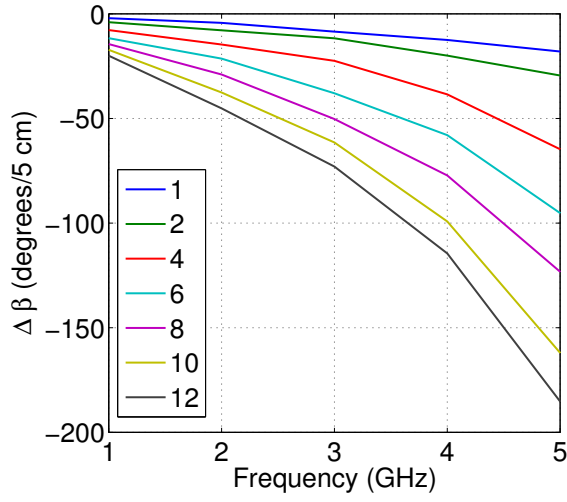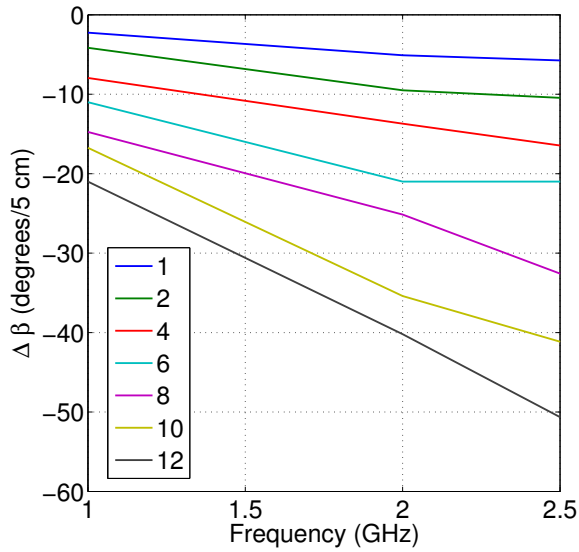
Figure 4.34. Difference of β between the on and off states of the VEPSs up to 2.5 GHz in ADS
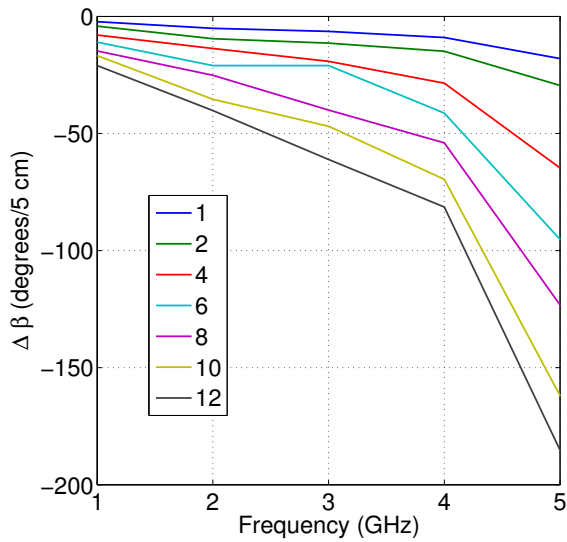
Figure 4.35. Difference of β between the on and off states of the VEPSs up to 5 GHz in ADS

into the VEPS, you can increase the amount of phase change introduced, as well as increase the effective permittivity, from this data one can accurately decide on the number of MRSs to embed within the VEPS to achieve a desired phase shift or ϵ_{reff}. Next, VEPSs with one embedded MRS and 12 embedded MRSs will be manufactured and compared to the results from simulations.
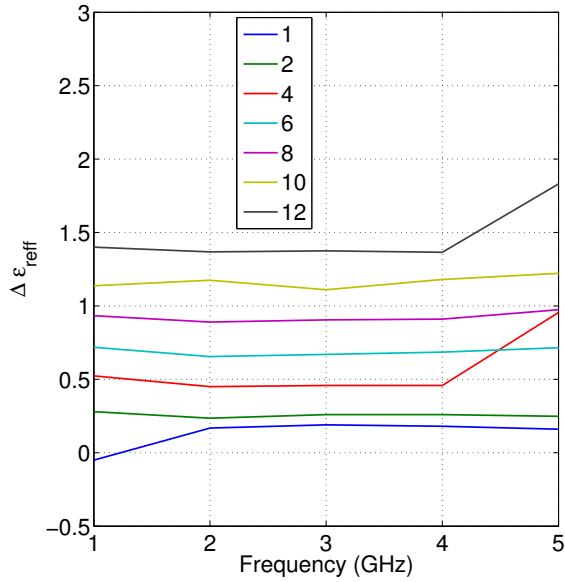
Figure 4.36. Difference of ϵ_{reff} between the on and off states of the VEPSs in ADS

4.5. Manufactured Boards

4.5.1. Manufacturing Process

Following the architecture of the VEPS given in Section 4.2, the layers for the VEPS were milled in house at North Dakota State University on Rogers TMM4 with substrate thicknesses of 20 mils. The milled top layer can be seen Fig. 4.37 where the trace is shown on the left and the non cladded back is shown on the right. This was the board used for the 12 embedded MRSs, an identical board was used for the single MRS. The bottom layers for the VEPSs with 12 embedded MRSs and one embedded MRS can be seen in Fig. 4.38 (a) and (b), Where Fig. 4.38 (a) shows the one embedded MRS for the top (left) and bottom (right) planes and Fig. 4.38 (b) shows

Figure 4.37. Milled top layer for the VEPS with the 50 Ω trace on the left and the non-cladded back on the right

41

(a)

(b)
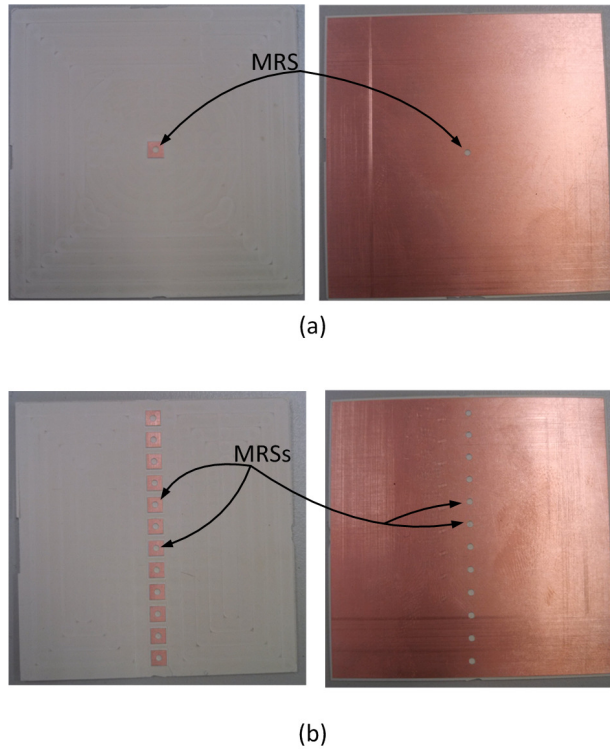
Figure 4.38. Milled top layer for the VEPS with the 50 Ω trace on the left and the non cladded back on the right

the 12 embedded MRSs for the top (left) and bottom (right) planes. Next, a layer of copper foil and copper tape was placed over the bottom side of the MRSs, before they were filled with the conductive micro size magnetic particles through the top. Finally, the top of the bottom substrate was covered with copper foil and tape, followed by stacking the two substrates and soldering SMA connectors on both ends for measurements. The finished VEPS are shown in Fig. 4.39 (a) and (b), where Fig. 4.39 (a) shows the top view of the boards, the VEPS with 12 embedded MRSs on the left and the VEPS with one embedded MRS on the right. And Fig. 4.39 (b) shows the bottom view, where the copper tape overlaying the bottom end of the MRSs can be seen for 12 MRSs (left) and 1 MRS (right).

4.5.2. Measurement Process

Due to the high frequencies being used, a controlled environment was desired for testing, so the VEPSs were measured in an anechoic chamber that absorbs RF within it and blocks RF from entering the chamber. Using a network analyzer, the VEPS were measured three times in both the off and on states using small cylindrical permanent magnets, due to their magnetic field lines
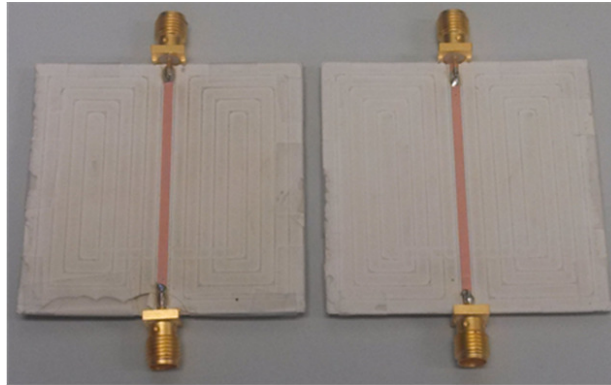
(a)
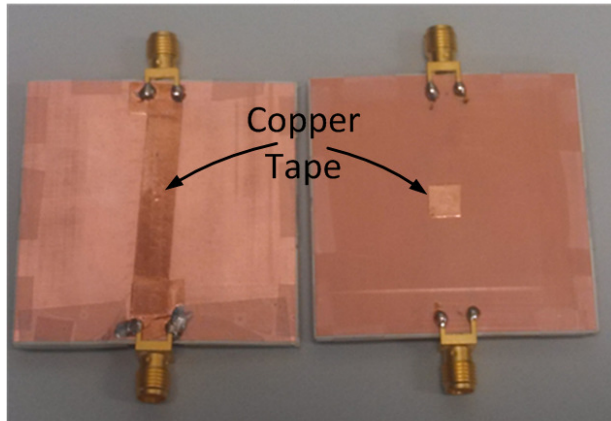
(b)

Figure 4.39. Assembled VEPS with (a) a top view of the VEPS with 12 embedded MRSs (left) and one embedded MRS (right) and (b) a bottom view of the VEPS with 12 embedded MRSs (left) and one embedded MRS (right), where overlaying copper tape can be seen.
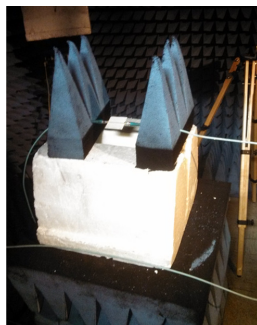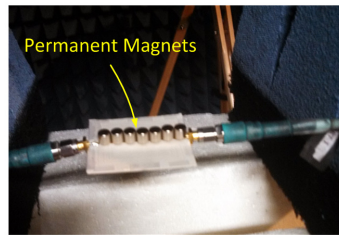
(a)   (b)

Figure 4.40. Anechoic Chamber with (a) expanded view of deactivated VEPS and (b) close up view of activated (VEPS)

moving vertically through the substrate as opposed to horizontally. the average of the three runs was taken as the result data. The anechoic chamber with a deactivated VEPS can be seen in Fig. 4.40 (a) next to an activated VEPS shown in Fig. 4.40 (b).

4.6. Measurements compared to Simulations

Following the same procedure as ADS and HFSS, S-parameters, the phase constant (β), the and effective permittivity (ϵ_{reff}) were plotted. Shown in Fig. 4.41 is the reflection coefficient of a single embedded MRS within the VEPS. Here it can be seen that HFSS and ADS present very similar results in both the on and off states, while the measurements differ. However, it should be noted that the measurements act consistently with simulations, when in the off state, $|S_{11}|$ is below -10 dB past 5 GHz. When in the on state, $|S_{11}|$ shifts up, in this case measurements showing a good reflection coefficient (below -10 dB) up to 1.7 GHz. The $|S_{12}|$ values can be seen in Fig. 4.42 where it is shown that the single embedded MRS has a $|S_{12}|$ parameter of greater than -3 dB in the on state up to 4.7 GHz. The $|S_{11}|$ and $|S_{12}|$ for 12 embedded MRSs share similar consistencies and are shown in Figs. 4.43 and 4.44, respectively. Next, the phase for 1 and 12 embedded MRSs is shown in Figs. 4.45 and 4.46 where a consistent phase shift is seen between the on and off states for ADS, HFSS, and measurements for both a single MRS and 12 embedded MRSs. Although results don't exactly match with simulations, this is still a very important find. Current methods of adjusting changing the phase either involve directly connected components (such as a varactor diode) or a permanent and irreversible change (such as a mushroom structure).
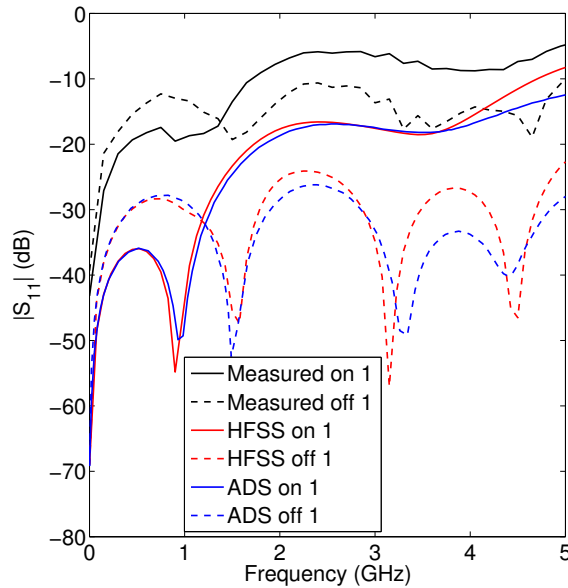
Figure 4.41. $|S_{11}|$ comparisons between HFSS, ADS, and measurements, $|S_{22}|$ is similar to $|S_{11}|$ for one embedded MRS
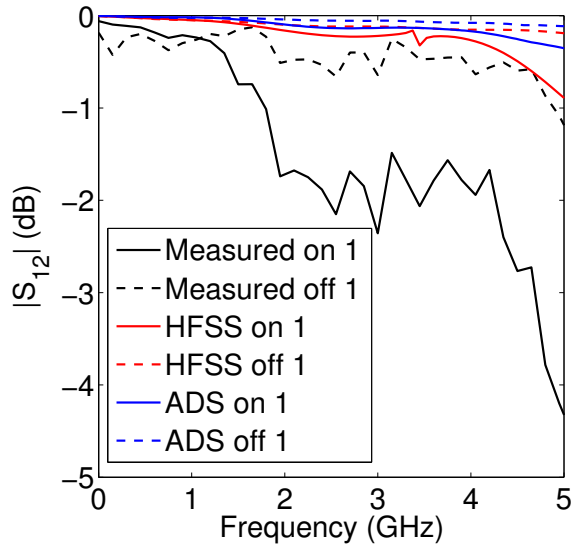
Figure 4.42. $|S_{12}|$ comparisons between HFSS, ADS, and measurements, $|S_{21}|$ is similar to $|S_{12}|$ for one embedded MRS

These results indicate we can adjust the phase without connecting to the TL. They also indicate we have constructed a reconfigurable structure, where we can turn the VEPS on or off as we desire to achieve certain phase characteristics. This can be more clearly seen in the phase constant (β)
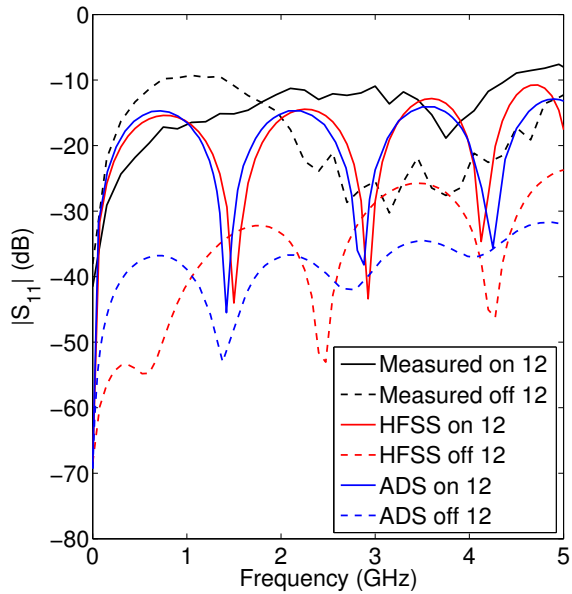
Figure 4.43. $|S_{11}|$ comparisons between HFSS, ADS, and measurements, $|S_{22}|$ is similar to $|S_{11}|$ for 12 embedded MRSs

.
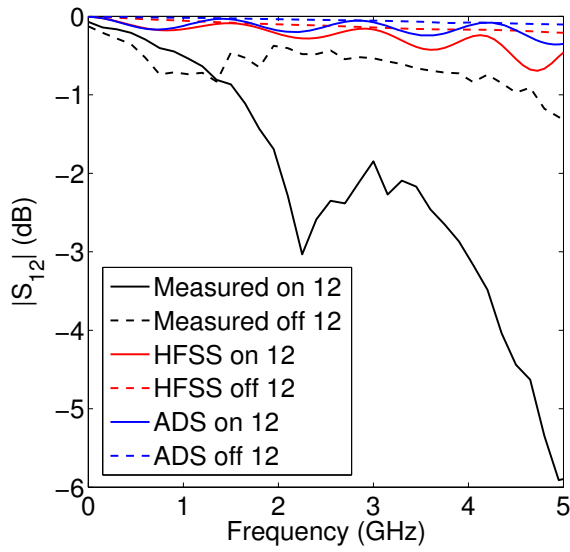
Figure 4.44. $|S_{12}|$ comparisons between HFSS, ADS, and measurements, $|S_{21}|$ is similar to $|S_{12}|$ for 12 embedded MRSs

plots shown in Figs. 4.47 and 4.48. Notice in Fig. 4.47 that there is a much smaller change in β as compared to Fig. 4.48. This result was expected and desired, as it allows for controlling the amount of phase introduced with each MRS, allowing for more precise phase shifts and design
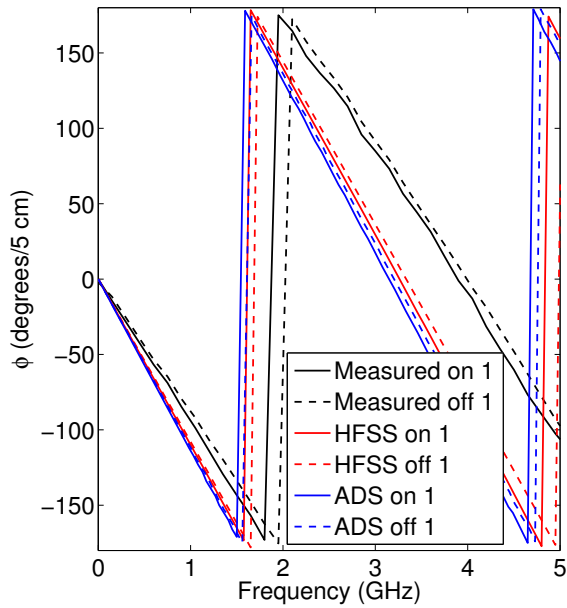
Figure 4.45. Phase comparisons between HFSS, ADS, and measurements for one embedded MRS
.

Figure 4.46. Phase comparisons between HFSS, ADS, and measurements for 12 embedded MRSs
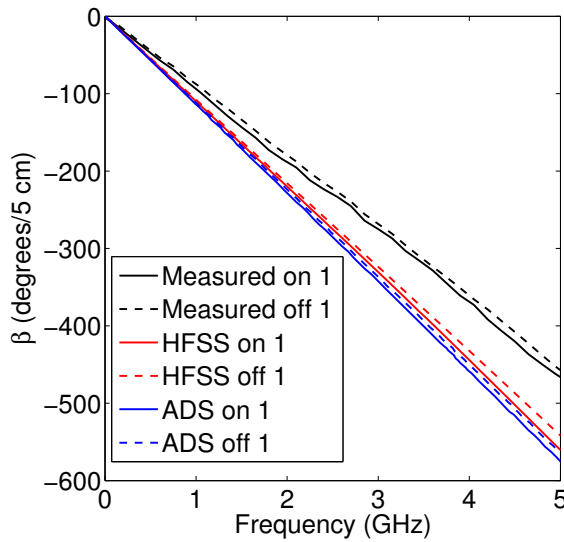
Figure 4.47. β comparisons between HFSS, ADS, and measurements for one embedded MRS

.

standards. The change in β also affects the change in the ϵ_{reff} as shown in Figs. 4.49 and 4.50. It should be noted that the ϵ_{reff} for the measured results in the off state is around 2.15. This value is much lower than the simulated and online calculated values around 3.4, and reasons for this will

be covered in the Discussions section. Finally, taking the difference between the on and off states for β and ϵ_{reff} resulted in Figs. 4.51 and 4.52, respectively.

4.7. Discussion

It can be seen from Figs. 4.51 and 4.52 that the difference (Δ) for the single embedded MRS is very close in value to the Δ for both HFSS and ADS. It can also be seen that the Δ for the 12 embedded MRSs share a pattern in increasing the ϵ_{reff} when activated. Patterns for measurements and results are consistent when values increase and decrease, the mismatch in values could be caused by a number of reasons, and a few will be discussed here.

The first possibility is the milled TMM4 boards. Starting with a substrate height of 20 mils, there was little substrate to be milled from. When the milling machine mills the copper cladding, it also digs into the substrate slightly. Even if that distance is only 3 or 4 mils, the VEPS consisted of two separate boards and each board was milled separately. The top substrate, consisting of the 50 Ω trace, was milled on both sides while the bottom substrate was milled on only one side. Between these three mills, that may take over 10 mils from the overall VEPS height, approximately 25% of the entire height. This effect would significantly affect the results by lowering the characteristic impedance Z_o, which was seen in the S-parameter plots.
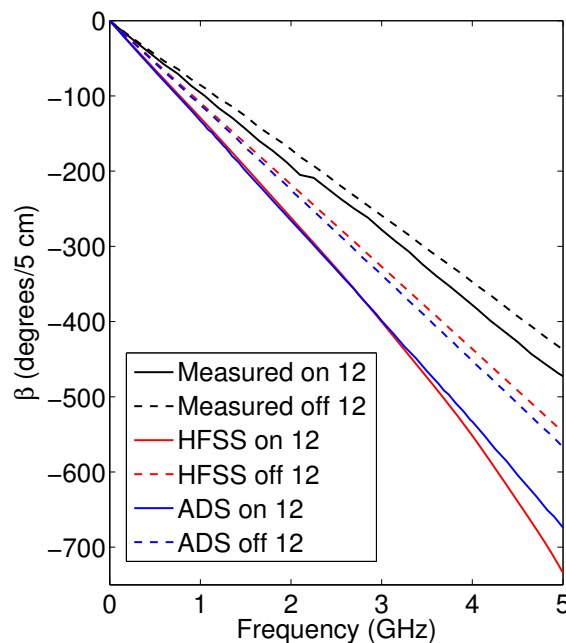
Figure 4.48. β comparisons between HFSS, ADS, and measurements for 12 embedded MRSs
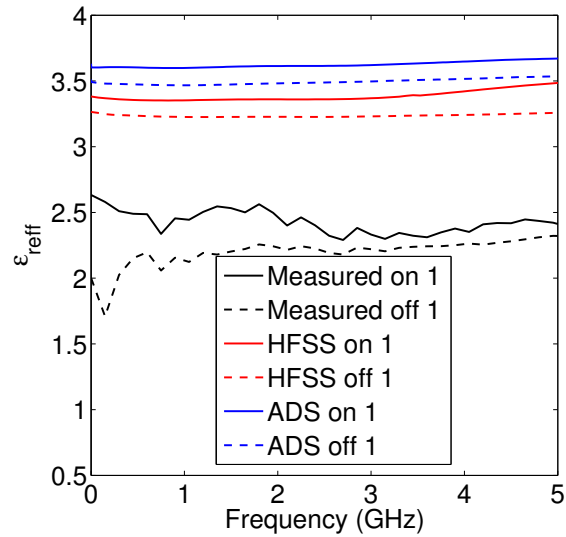
Figure 4.49. ϵ_{reff} comparisons between HFSS, ADS, and measurements for one embedded MRS

The second possibility is the air gap between the top and bottom substrates of the VEPS. Even at a minimal size of a few mils compared to the size of the VEPS being studied it is still significant. The ϵ_r of air is approximately 1, which is much lower than the $\epsilon_r = 4.5$ of the material

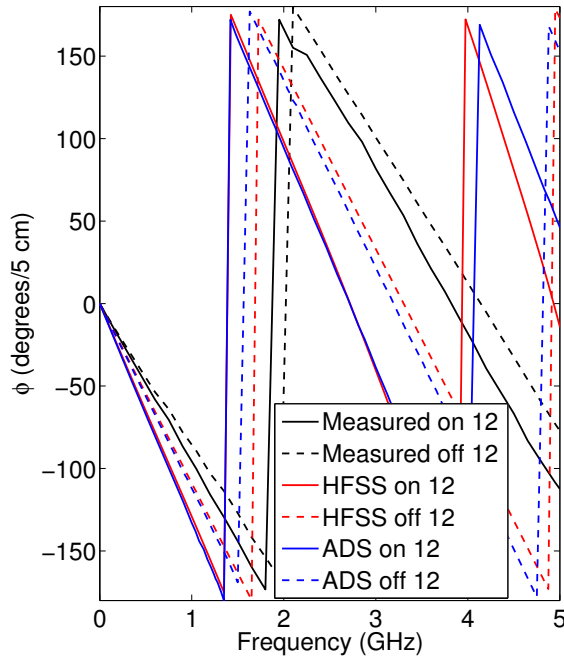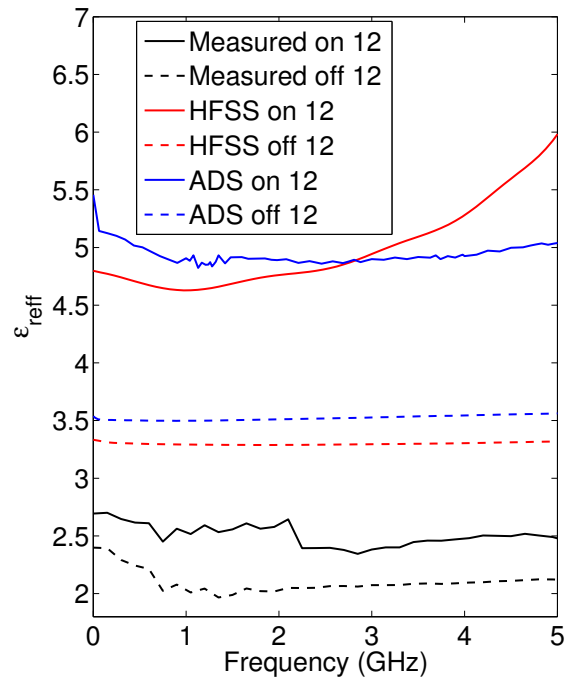Figure 4.50. ϵ_{reff} comparisons between HFSS, ADS, and measurements for 12 embedded MRSs
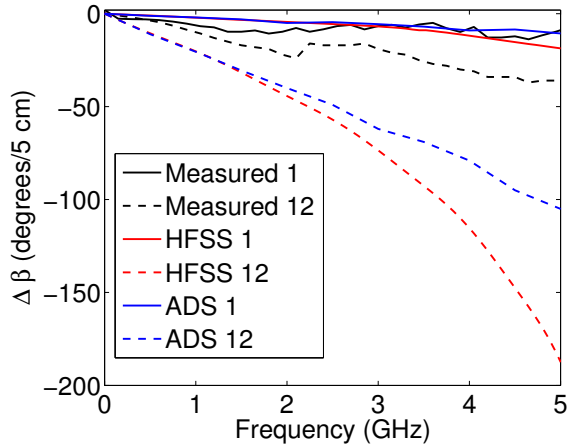
Figure 4.51. β Difference comparisons between HFSS, ADS, and measurements

we are using. The air gap could be a reason for the small ϵ_{reff} that was measured.

A third possibility has to do with the activation of the MRSs. Although a difference was noticed with and without the magnetic field present, there has been no perfect way to determine if the MRSs are activated without adding extra wiring or altering the structure used. This presents itself as more of an issue with the VEPS that had 12 embedded MRSs. Although there was a noticeable change, more so than a single embedded MRS, it is unknown whether all 12 of the MRSs were activated, or if a smaller amount was activated.

Among these reasons, standard error including equipment, material, environmental at-
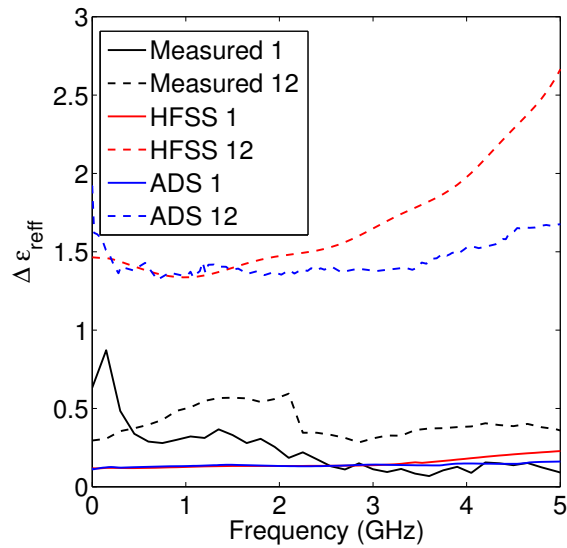
Figure 4.52. ϵ_{reff} Difference comparisons between HFSS, ADS, and measurements

tributes, and real-world error all may contribute to the discrepancy. However, it is the author's belief that the primary reasons are due to the three specifically mentioned. To account for this error, one could develop the VEPS on a thicker substrate where milling thickness, and air gaps would have less of an influence. No suggestions are available on how to handle the problem of knowing whether or not an MRS is activated without connecting direct wires.

4.8. Conclusions

The magneto-static responsive structures (MRSs) were embedded into a variable effective permittivity structure (VEPS) with the intent of controlling the phase constant β and effective permittivity ϵ_{reff} of the structure. By introducing a magnetic field, the MRSs could be activated changing the characteristics of the VEPS. The VEPS were simulated in the computer programs HFSS and ADS, followed by measuring manufactured boards. Results showed similar patterns between simulations and measurements, however some discrepancies existed in values comparing simulations and measurements. It is the author's belief that these discrepancies are due primarily to the manufacturing method and board thickness of the substrates used. Results have still shown the ability to reconfigure β and ϵ_{reff} without directly connecting to the transmission line like some current methods. This shows promise in the future of this technology as more of its characteristics are determined and practiced.

5. OTHER WORK BRIEFLY STUDIED

5.1. Introduction

This chapter is an initial investigation of new applications for the magneto-static responsive structure (MRS). Many improvements can still be made increasing the efficiency, decreasing the size, and developing better methods for manufacturing the MRS. This chapter is going to provide a summary of some areas that were briefly studied by the author, as well as other suggestions for those that may wish to continue this work.

5.2. Geometry of the Magneto-Static Responsive Structure

As presented in Chapter 2, the MRS has a good match (under -10 dB) past 3.0 GHz in the on state, and $|S_{12}|$ under 10 dB in the off state up to about 300 MHz. As shown in Figs. 2.7 and 2.8. It is at these boundaries that the capacitance of the structure starts dominating, diminishing the ability of the MRS to function as a switch. However, it is known by the equation presented in Chapter 2

$$C = \frac{\epsilon_r \, \epsilon_o \, A}{h} \tag{5.1}$$

that the capacitance relies on the relative permittivity (ϵ_r), cross sectional area (A) and the height (h) of the MRS. Therefore, to decrease the capacitance we could decrease ϵ_r or A, as well as increase h. All substrates used in this paper were Rogers TMM4 ($\epsilon_r = 4.5$) so another substrate with a lower ϵ_r, such as Rogers 5880 ($\epsilon_r = 2.2$) or Rogers TMM3 ($\epsilon_r = 3.27$) could easily be chosen. Also, all MRSs used had side lengths of 3.0 mm, giving them a cross sectional area A = 9.0 mm^2 shown in Fig. 5.1 (a). Further reduction in side length would decrease the capacitance and some reduction has already been shown in [25] and can be seen in Fig. 5.1 (b). Comparisons between the 3.0 mm and 1.5 mm MRSs can be studied in [25], where it is evident that a decrease in the side length (l) vastly increases the performance of the MRS. Even more reduction in side length shown in Fig. 5.1 (c) could be studied to increase the performance of the MRS. Finally, an increase in the height of the MRS would further reduce the capacitance, many switches described in this paper had a height h = 0.508 mm, much taller MRSs could operate better.
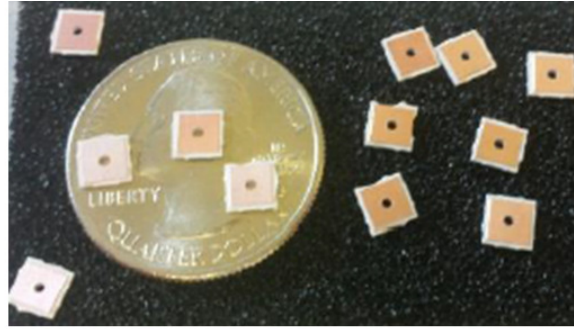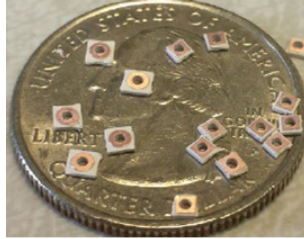
Figure 5.1. Varying MRS sizes: (a) Side length l = 3 mm as studied in this work, (b) Side length l = 1.5 mm as studied in [25], (c) Side length l = 1 mm as proposed work

5.3. Magnetic Particles

The silver coated magnetic particles used in this work was the Potters Industries SM40P20 (Fig. 5.2) [26]. These particles had an average micron size of about 40, but ranging anywhere
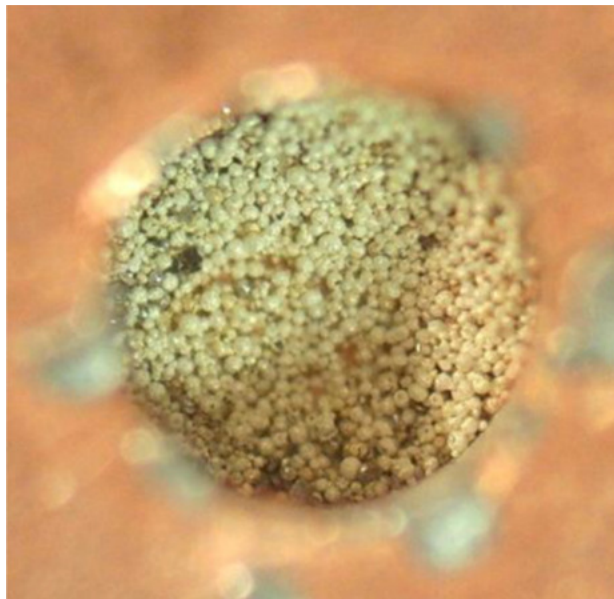
Figure 5.2. SM40P20 Magnetic Particles: It can be seen the particles have widely varying sizes

between 10 to 70 um. This inconsistency in size made determining particle amount difficult and required manually counting and measuring cups for semi-accurate numbers. If the particles were more consistent in size, then other filtering methods could be used to determine the amount of particles in a more effective and precise manner. Also, the size of the particles was fairly large compared to some products on the market (some conductive magnetic particles have sizes in the nano meters) so a decrease in size of the particles would allow for easier activation with a smaller magnetic field. Something that will be covered further in the next section.

5.4. Activation Methods

This work depended completely on activation methods by the use of permanent magnets. While the activation of the switch using a permanent magnet works nicely within certain fields of study and still have advantages over a typical MEMS or Pin diode configuration, optimization can still be made. To proceed with our current design and use the MRS as an actual switch, we would have to be able to introduce a magnet to turn the switch on, or take away the magnet to turn the switch off. This method closely resembles that of a typical MEMS, but further work in activation methods would increase the effectiveness of the MRS. It is possible to create a magnetic field using well known physical structures, as suggested in the next few sections.

5.4.1. Spiral Transmission Line

The first possible structure would be a spiral transmission line (TL) milled out of the ground plane of the MRS as shown in Fig. 5.3. Using the right hand rule (RHR), we can create a magnetic field in the center of the spiral by connecting it to a DC source, providing current traveling down the TL, and therefore a magnetic field. Attempts were unsuccessful in accomplishing this with the
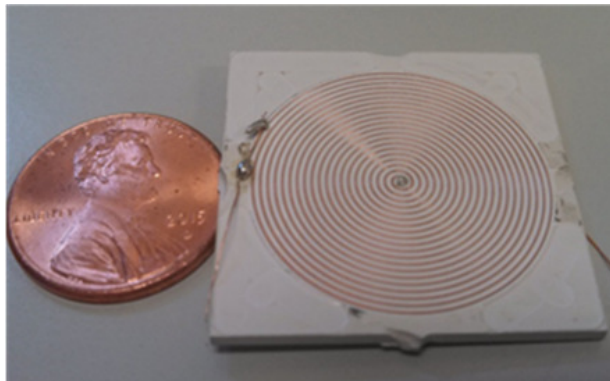
Figure 5.3. Prototype microstrip spiral TL for activating the MRS
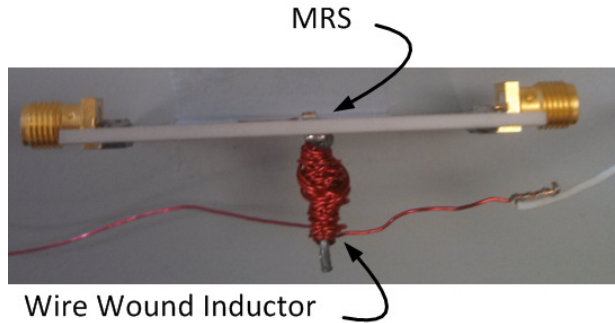
Figure 5.4. Hand-winded inductor for activating the MRS

current equipment setup, as the magnetic field created by the TL was not strong enough to stack the particles. As described in the section covering Magnetic Particles, a smaller particle size would require a smaller magnetic field to feel the affect, giving the hypothesis that if smaller particles were used, the spiral TL shown could have been successful in activating the MRS.

5.4.2. Wire-Wound Inductor

The second possible structure would be a wire wound inductor. Using similar principles as the spiral TL, it has been shown that a wire wound inductor has the ability to activate the MRS. Using the structure shown in Fig. 5.4, the MRS was activated with a voltage as low as 241 mV with a current of 250 mA. Requiring a total amount of power P = 60 mW. This is a very low power required compared to current switching methods, such as Pin diodes that can require 700 mV for biasing and 300 mA (P = 210 mW). Regarding the structure in Fig. 5.4, it has approximately 250 wraps around the thin metal, even then, it can be gathered that this design is quite primitive. Commercial bobbin wound inductors can be bought and tested, connecting the inductor closer to
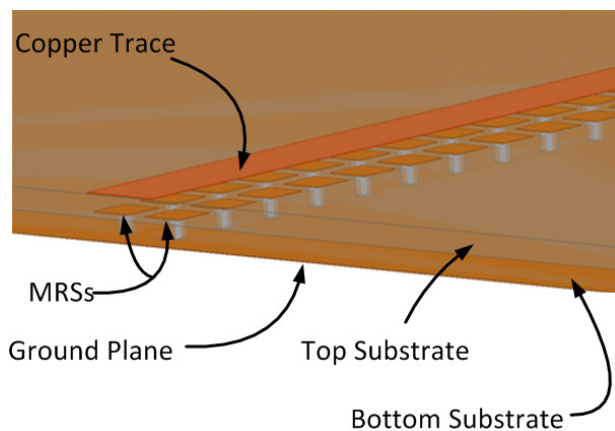
Figure 5.5. Screenshot of the HFSS simulated VEPS with 66 embedded MRSs

Figure 5.6. $|S_{11}|$ of the VEPS with 66 embedded MRSs in the on and off states, $|S_{22}|$ is similar to $|S_{11}|$

the MRS with more coil winds closer together. Possibly allowing for even lower activation voltages and currents of the MRS.

5.5. Different Size MRSs Embedded within the VEPS

The primary MRSs studied this far have had a size of 3 x 3 mm. While studies have determined the effectiveness of a smaller MRS, the smaller MRS has not been embedded within the VEPS for a study of the characteristics. Shown in Fig. 5.5, we have simulated a VEPS embedded with 66 MRSs with side length l = 1.0 mm and cavity diameter d = 0.4 mm, and a gap of 0.25 mm between them. The S-parameters of this VEPS can be seen in Figs. 5.6 and 5.7. Unlike before,
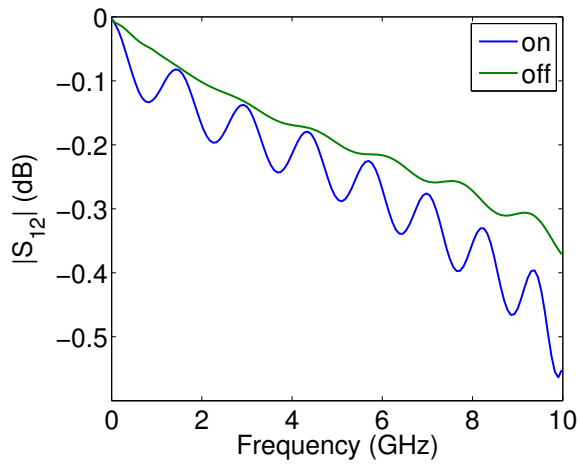
Figure 5.7. $|S_{12}|$ of the VEPS with 66 embedded MRSs in the on and off states, $|S_{21}|$ is similar to $|S_{12}|$
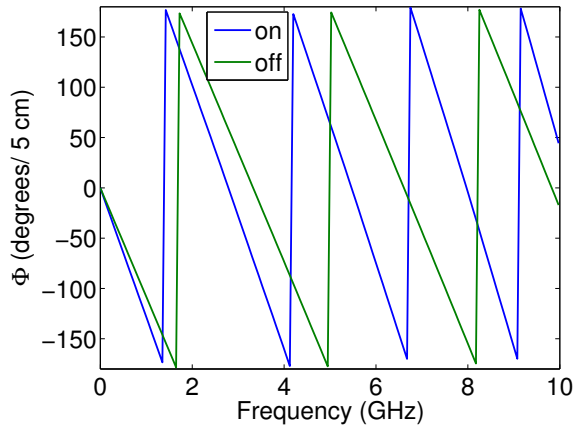
Figure 5.8. Phase of the VEPS with 66 embedded MRSs in the on and off states

here the inductance and capacitance seem to be matched very well, where the VEPS is no longer blocking power at higher frequencies. This can be further seen in the phase plot shown in Fig. 5.8 which shows a clean frequency shift between the on and off states all the way up to 10.0 GHz. We can further plot the phase constant β and the effective permittivity ϵ_{reff} giving us Figs. 5.9 and 5.10, respectively, that show a uniform shift for the entire frequency range in both plots. Finally, a difference between the on and off plots for Figs. 5.9 and 5.10 can be seen in Figs. 5.11 and 5.12. Fig. 5.11 shows a clean change in β for the entire frequency shift. Perhaps the more useful result shown in Fig. 5.12 displays a near uniform change in the ϵ_{reff} ranging from 1.3 to 2.2. This is an interesting result as it negates the primary effect of the frequency, allowing for a consistent affect on ϵ_{reff} throughout the entire frequency sweep. One such application where this may be useful,
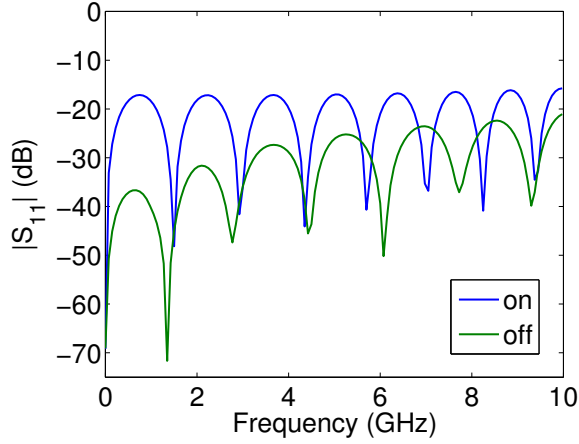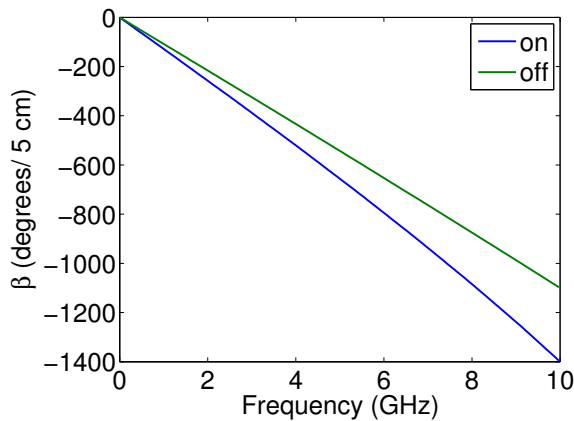

Figure 5.9. β of the VEPS with 66 embedded MRSs in the on and off states

57
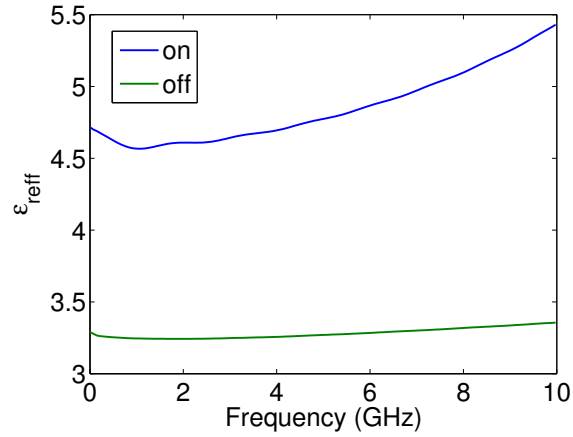
Figure 5.10. ϵ_{reff} of the VEPS with 66 embedded MRSs in the on and off states
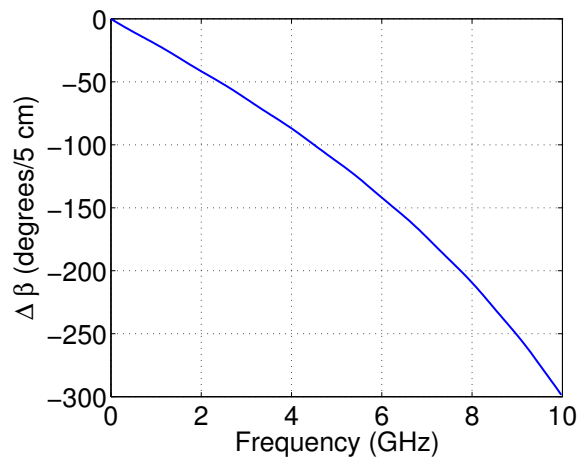
Figure 5.11. Difference of the β of the VEPS with 66 embedded MRSs in the on and off states
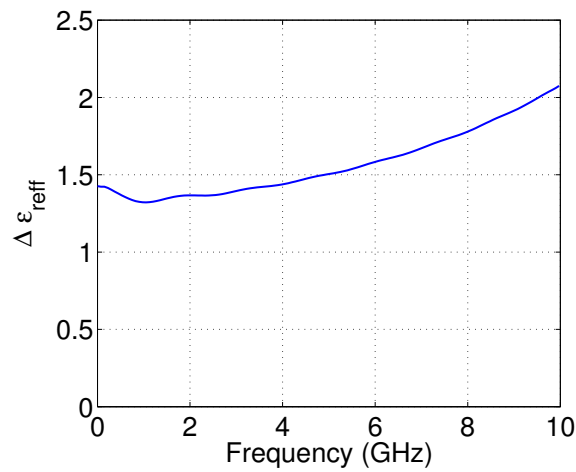
Figure 5.12. Difference of the ϵ_{reff} of the VEPS with 66 embedded MRSs in the on and off states

is for materials with a higher permittivity that need to be adjusted slightly. For example, Rogers TMM13i has a relative permittivity (ϵ_r) of about 12.85, with no standard materials having a higher ϵ_r. With the introduction of this VEPS with these embedded MRSs, the effective permittivity of that material could be increased without affecting it's other properties, something that can be very useful in many circumstances.

6. CONCLUSIONS

A study of several characteristics of the new magneto-static responsive structure (MRS) has been conducted here. First, a lumped circuit model of the MRS was proposed and modeled as two separate HFSS geometries, one using a generic modeling procedure, the other using HFSS lumped RLC boundaries. Results showed excellent comparisons between measurements and the separate HFSS simulations up to 3.0 GHz, verifying the accuracy of the lumped circuit model. Next, ringing and overshoot characteristics of the MRS were studied and compared with those of the widely used Pin diodes. From the measurement comparisons, it can be seen that the MRS is much less lossy then the Pin diodes, while the MRS has similar bandwidth measurements to the continuous TL, where the Pin diode is closer to the continuous TL only at 40.0 Mhz. Showing that the MRS is more efficient as a RF switch than the Pin diode. Finally, the MRS was constructed in a fashion as to achieve a variable effective permittivity (ϵ_{reff}). By embedding the MRS into a structure, a variable effective permittivity structure (VEPS) was created allowing for reconfigurability of the phase constant β and ϵ_{reff} without direct connections to the transmission line. Results showed proof of this ability, and were comparable to computer simulations using HFSS and ADS. Finally, several studies revolving around the MRS were investigated. An introduction to size dimensions and optimization of the MRS was proposed, calculations were given as suggestions for altering the ability of the MRS as a radio frequency (RF) switch. A suggestion to the advantages of using more consistent, smaller magnetic particles was given, along with advantages to using them. Different activation methods were proposed, one using a micro strip TL on the ground plane of the substrate, the other using a wire-wound inductor vertically facing the MRS. Both methods revolve around the right-hand rule by creating a strong magnetic field down the center of the spiral. Activation of the MRS was achieved with 60 mW of power through the use of a hand-wound wire inductor. The final brief study involved using more of the smaller MRSs embedded into the VEPS. Through the use of HFSS, a balanced L and C structure was simulated that had a good reflection coefficient past 10 GHz in both the on and off states. Finally, the appendix includes enlarged figures of several plots presented in Chapter 4. A useful tool for referencing when designing with the MRSs.

REFERENCES

[1] F. Yang, and Y. Rahmat-Samii, "A Reconfigurable Patch Antenna using Switchable Slots for Circular Polarization Diversity", *IEEE (MWCL)*, Vol. 12, Issue 3, March 2002, pp.96-98.

[2] S. Sharma, M. Gupta, and C.C. Tripathi "Reconfigurable Antenna: A Review", *International Journal of Electronics and Communication Technology*, Vol.2, Issue 3, Sept. 2011

[3] J. T. Bernhard, R. Wang, R. Clark, and P. Mayes "Stacked Reconfigurable Antenna Elements for Space-based Radar Application", *IEEE AP-S International Symposium*, Vol.1, 2001, pp.158-161

[4] J.C. Chiao, Y. Fu, I.M. Chio, M.Delisio, and L.Y. Lin, "MEMS Reconfigurable Vee Antenna" ,*Microwave Symposium Digest, 1999 IEEE MTT-S International*, Vol. 4, 1999, pp.1515-1518

[5] E. R. Brown, "RF-MEMS Switches for Reconfigurable Integrated Circuits" *IEEE Transactions on MTTs*, Vol. 46, November 1998, pp. 1868-1880

[6] J.C. Chiao, Y. Fu, D. Choudhury, and L. Y. Lin, "MEMS Millimeter Wave Components", *IEEE MTT-S International Microwave Symposium Digest, Anaheim, CA*, 1999, pp. 463-466.

[7] X. Yang, B. Wang, and Y. Zhang, "A Reconfigurable Hilbert Curve Patch Antenna", *IEEE AP-S International Symposium*, Vol. 2B, November 1979, pp. 613-616

[8] G. Huff, J. Feng, D. Zhang, and J. T. Bernard, "A Novel Radiation A Pattern and Frequency Reconfigurable Single Turn Square Spiral Microstrip Antenna", *IEEE (MWCL)*, Vol. 13, No. 2, January 2003, pp. 57-59.

[9] A. Mak, C. Rowell, R. Murch, and C. Mak, "Reconfigurable Multiband Antenna Designs for Wireless Communication Devies," *IEEE TAP.*, vol. 55, no. 7, Jul. 2007, pp. 1919-1928

[10] A. Mottershead, *Electronic Devices and Circuits.* New Delhi, India: Prentice-Hall of India, 2004

[11] Agilent. (2010, May 21). *Understanding RF/Microwave Solid State Switches and their Applications* [Online]. Available: http://cp.literature.agilent.com/litweb/pdf/5989-7618EN.pdf

[12] A. Kundu et al., "Cubic Structure SIC P-I-N Diode as RF Switch," Computational Intelligence and Information Technology, 2013. CIIT Third International Conference on, 2013,©IEEE. doi: 10.1049/cp.2013.2632

[13] E.W. Jacobs et al., "'Photo-injection PIN Diode Switch for High Power RF Switching," in Solid-State and Integrated-Circuit Technology, 2001. Proceedings. 6th International Conference on, 2013 ©IEEE. doi: 10.1109/ICSICT.2001.982133

[14] S. Nikolaou, "Pattern and Frequency Reconfigurable Annular Slot Antenna Using PIN Diodes," *IEEE TAP.*, Volume:54 , Issue: 2, pp. 439-448, Feb. 2006.

[15] I. Llama-Garro and Z. Brito-Brito, "Reconfigurable Microwave Filters, Microwave and Millimeter Wave Technologies from Phontonic Bandgap Devices to Antenna and Applications," *Minin (Ed.), InTech,* ISBN: 978-953-7619-66-4,pp.160-184,2010.

[16] E. Ojefors, S. Cheng, I. Skarin, P. Hallbjorner and A. Rydberg, "Electrically Steerable Single-Layer Microstrip Traveling Wave Antenna With Varactor Diode Based Phase Shifters," *IEEE TAP*, Vol. 55, NO. 9, pp. 2451-2460, Sept. 2007

[17] C. Caloz, A. Lai and T. Itoh, "Wave Interactions in a Left-Handed Mushroom Structure," *AP-S International Symposium*, vol. 2, June 2004, pp. 1403 - 1406

[18] W. Cao, B. Zhang, T. Uy, D. Guo and A. Liu, "Helical-Via-Type Mushroom EBG Structure for Size Reduction," *Mechanic Automation and Control Engineering (MACE), 2011 Second International Conference*, Hohhot, China, 2011, pp. 1347-1349

[19] T. Maruyama, J. Shen, N. Tran and Y. Oda, "Novel H-Type Mushroom-Like Structure for Multi-band Reflectarray," *Antennas and Propagation in Wireless Communications (APWC), IEEE-APS Topical Conference*, Torino, Italy, 2013, pp. 953-955

[20] A. Iftikhar, J. Parrow, S. Asif and B. Braaten., "On Using Magneto-static Responsive Particles as Switching Elements to Reconfigure Microwave Filters" *2016 IEEE IET Conference*, pp. , May 2016

[21] Z. BBrito, I. L-Garro, G. N-Muniz, J. P-Carrier, and L. Pradell, "UMTS-WIFI Switchable Bandpass Filter," *Proc. of the 39th European Microwave Conference*, pp. 125-128, Oct 2009.

[22] A. Iftikhar, J. Parrow, S. Asif, S. Sajal and B. Braaten., "Printed Dipole Reconfigured with Magneto-Static Responsive Structures without a Directly Connected Biasing Circuit" *IEEE AP-S/URSI*, pp. ,June 2016

[23] L. Gei and K. Luk, "A Band Reconfigurable Antenna Based on Directed Dipole," *IEEE TAP* Vol. 62, No. 1, Jan 2014, pp. 64-71.

[24] Ansys Inc., Ansoft HFSS, Version 15.0 [Online], http://www.ansoft.com, last access date: Jan 2015.

[25] A. Iftikhar, "Characterization of a Structure Consisting of MagnetoStatic Responsive Microscopic Particles and its Application in Antennas," Ph.D. dissertation, Dept. Elect and Comp Eng. North Dakota State Univ., Fargo, ND, 2015.

[26] Potters Industries, LLC, Conduct-O-FIL, [Online], http://www.pottersbeads.com, last access date: March 2016.

[27] R. Garg, I. Bahl and M. Bozzi, *Microstrip Lines and Slotlines, 3rd Ed.*. Norwood, MA :Artech House, 2013

[28] M. E. Goldfarb, R. A. Pucel, "Modeling Via Hole Grounds in Microstrip," *IEEE Microwave and Guided Wave Letters*, vol. 1, no. 6, June 1991, pp 135-137

[29] H. Johnson and M. Graham, *High-speed signal propagation: Advanced Black Magic*. Upper Saddle River, NJ: Prentice Hall PTR, 2002

[30] E. Bogatin, *Signal and Power Integrity-SIMPLIFIED 2nd Edition*. Ann Arbor, MI: Edwards Brothers, 2004

[31] W. Dally and J. Poulton, *Digital Systems Engineering*. Cambridge, NY: Cambridge University Press, 1999

[32] D. M. Pozar, "Transmission Lines and Waveguides" in *Microwave Engineering*, Fourth Edition, Hoboken, Wiley, 2012, ch. 3 pp147

[33] Brian C Wadell, Chemandy Electronics, [Online], http://chemandy.com/calculators/microstrip-transmission-line-calculator.htm, last access date: Feb 2016.

APPENDIX

This appendix includes enlarged versions of Figs. 4.21, 4.20, 4.22, 4.35, 4.34, 4.36, 4.51, and 4.52 for designing a variable effective permittivity structure (VEPS) with variable amounts of magneto-static responsive structures (MRSs) easier for computer programs HFSS, ADS, as well as measurements.
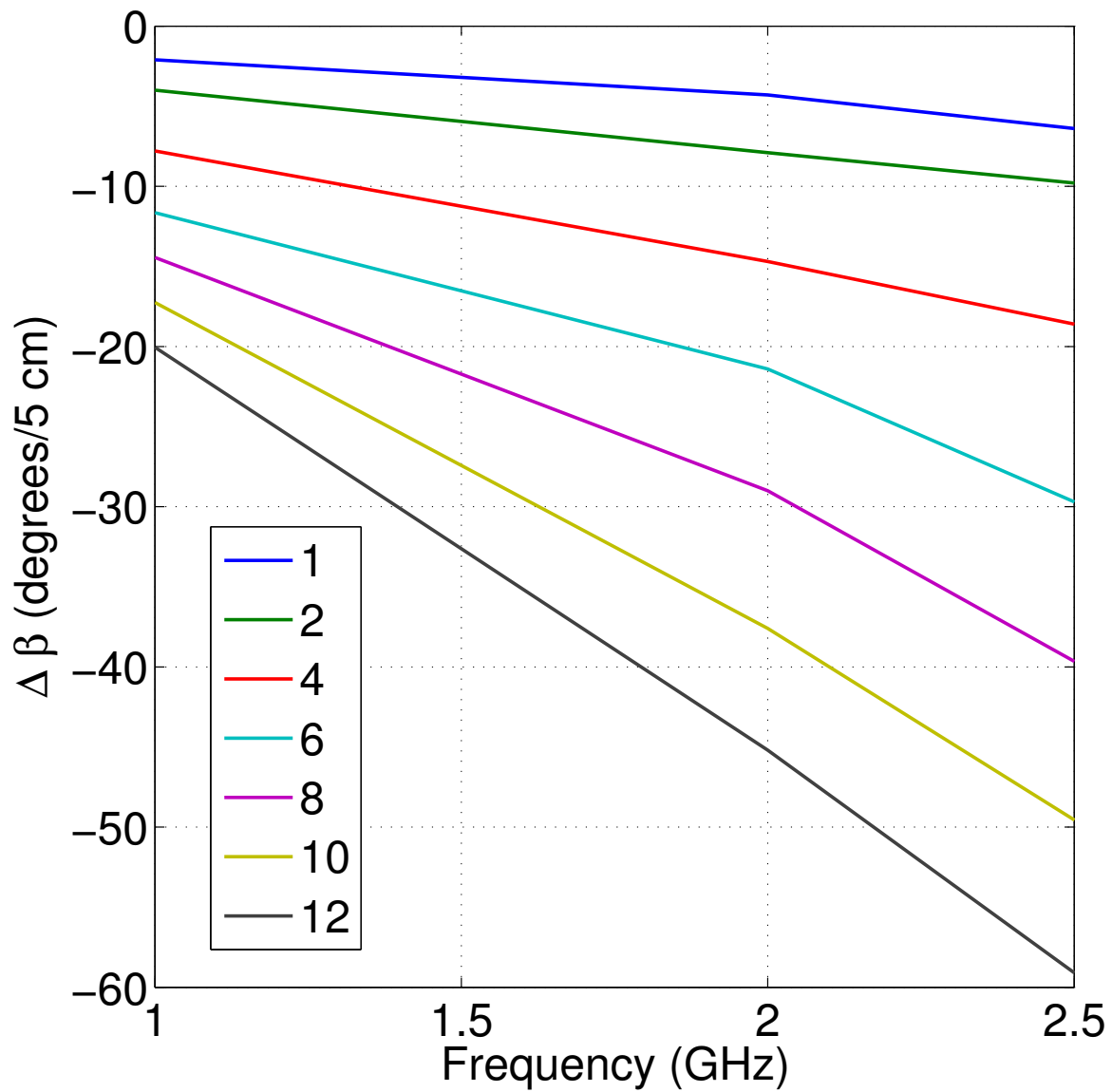
Figure A.1. Difference of β between the on and off states of the VEPSs up to 2.5 GHz in HFSS from Fig. 4.20
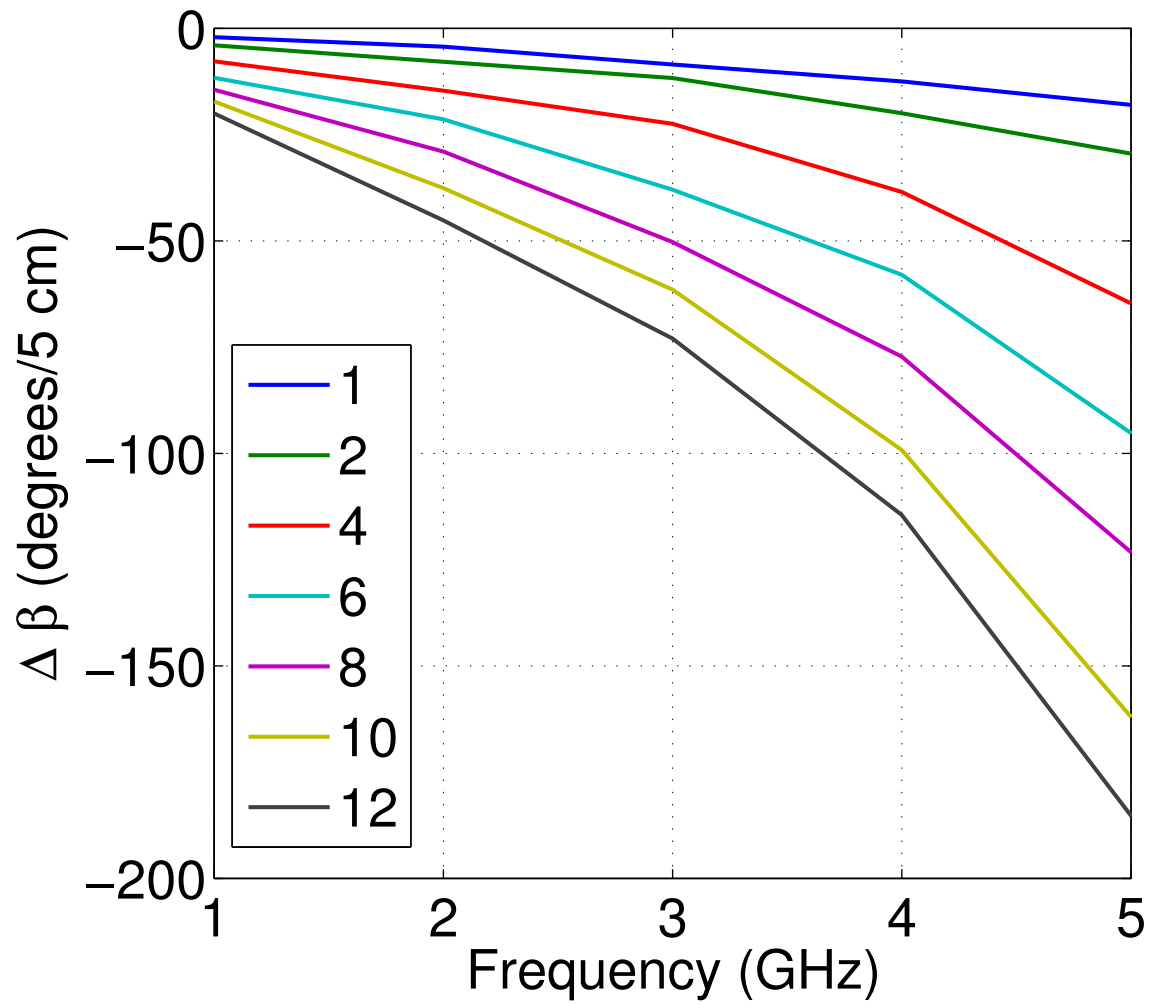
Figure A.2. Difference of β between the on and off states of the VEPSs up to 5 GHz in HFSS from Fig. 4.21
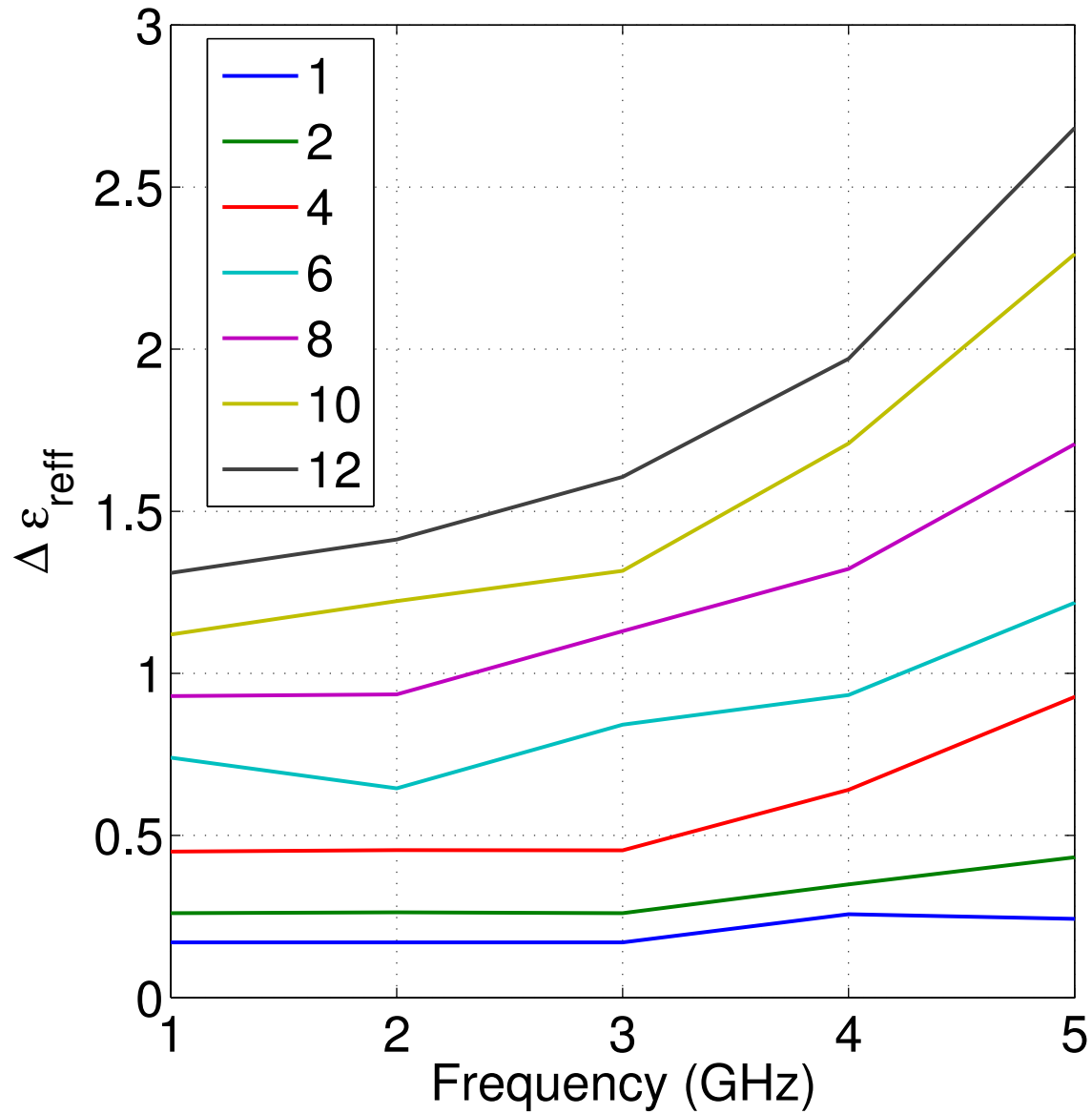
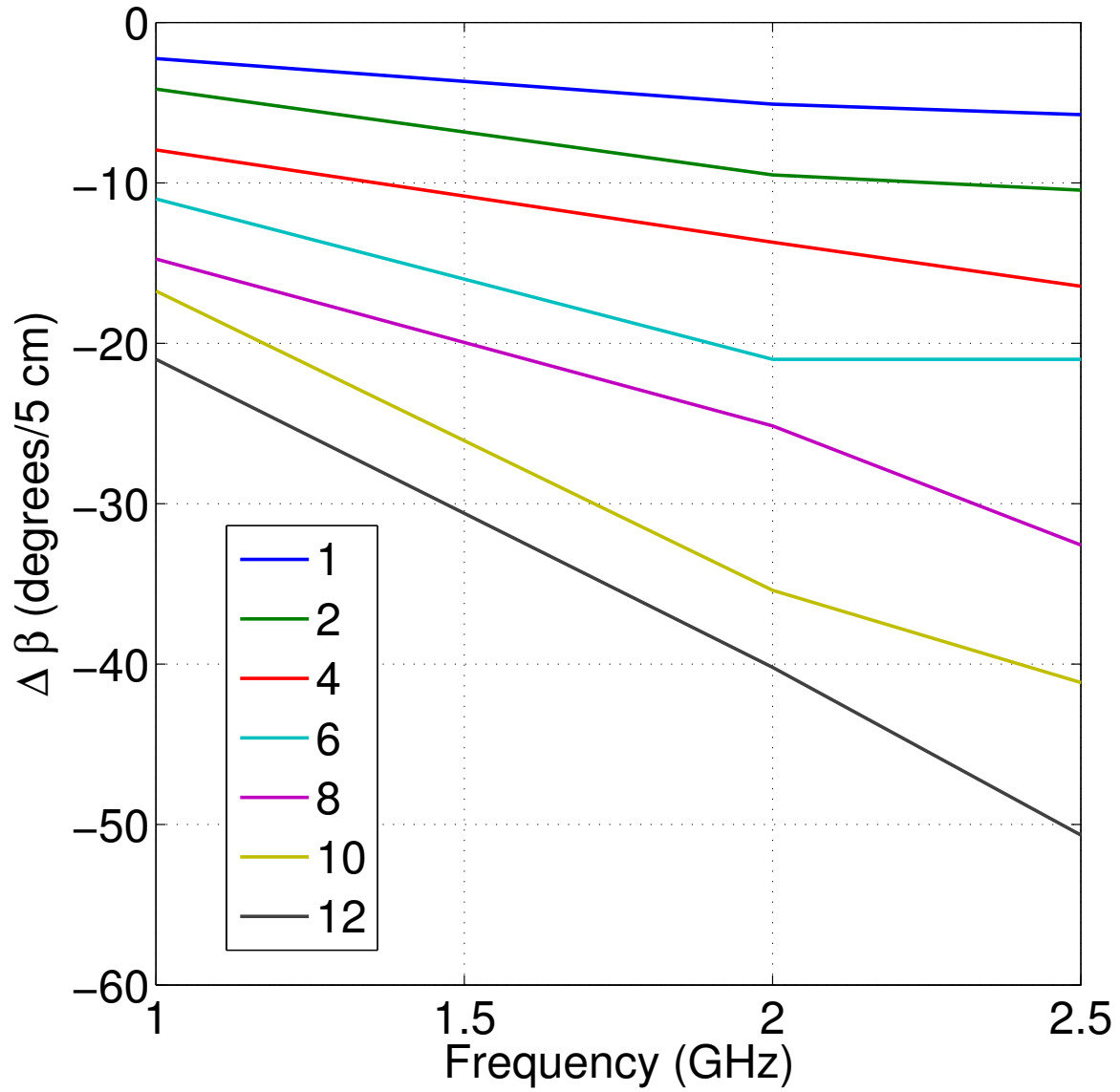Figure A.3. Difference of ϵ_{reff} between the on and off states of the VEPSs in HFSS from Fig. 4.22

Figure A.4. Difference of β between the on and off states of the VEPSs up to 2.5 GHz in ADS from Fig. 4.34
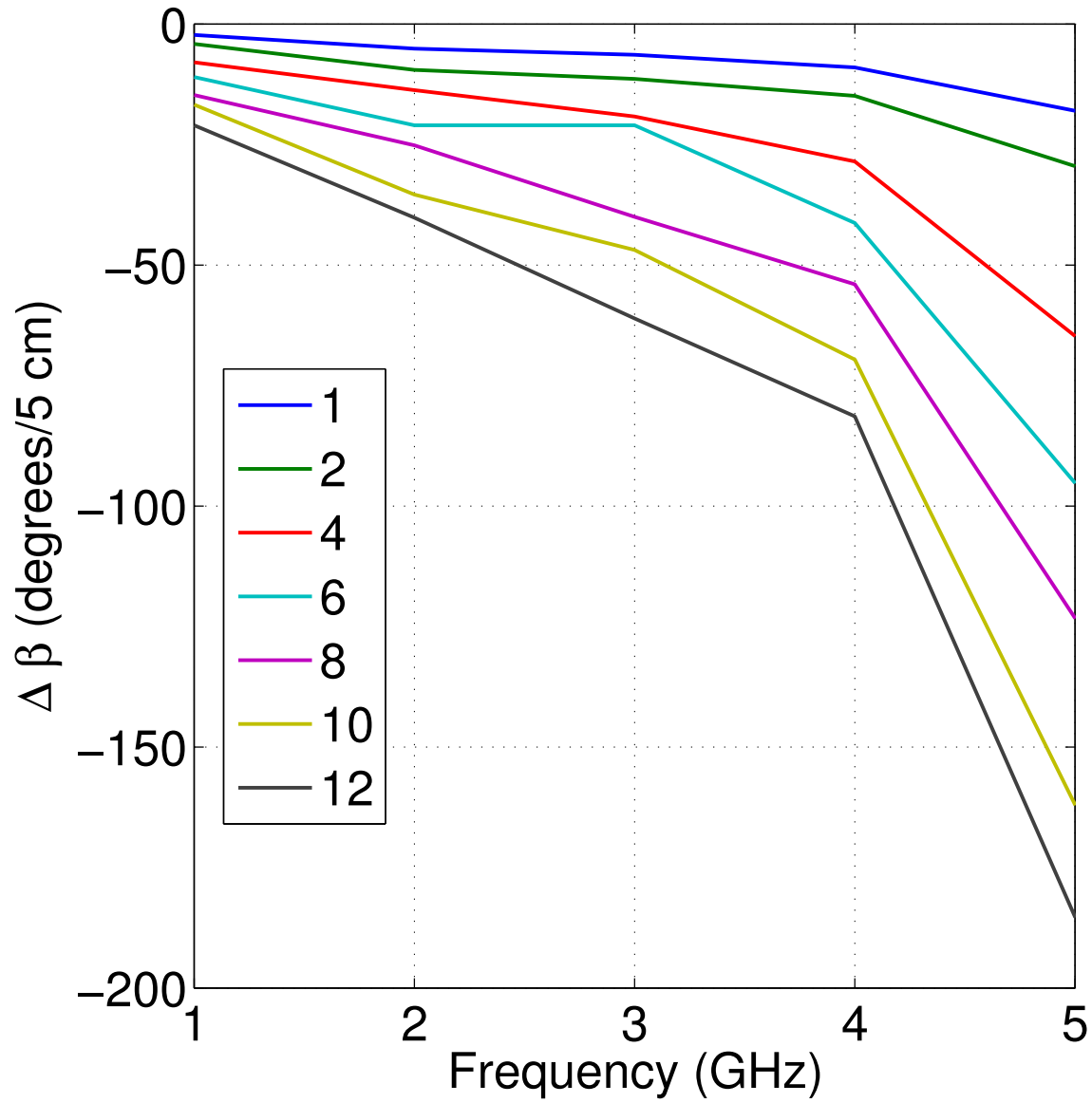
Figure A.5. Difference of β between the on and off states of the VEPSs up to 5 GHz in ADS from Fig. 4.35
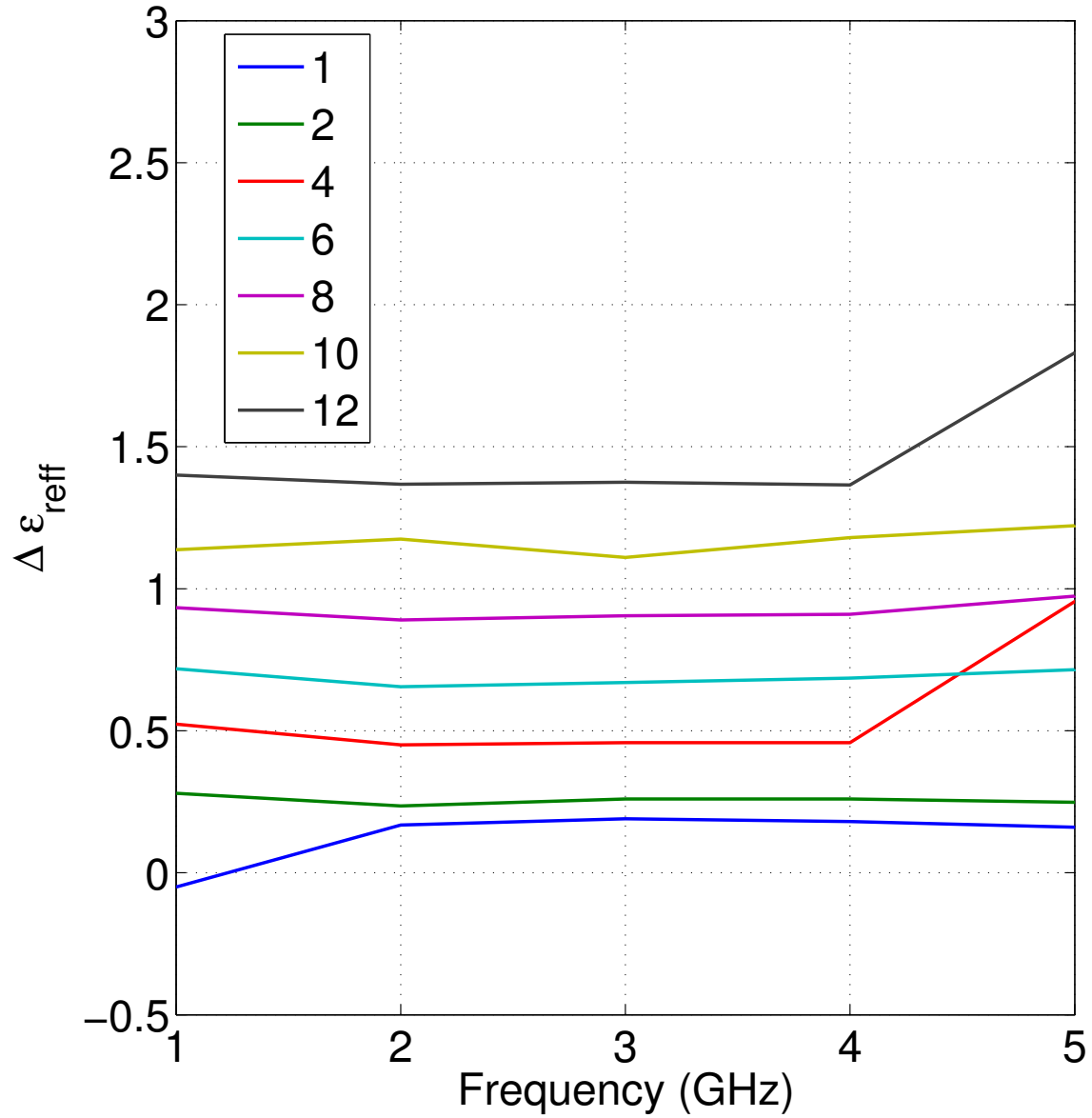
Figure A.6. Difference of ϵ_{reff} between the on and off states of the VEPSs in ADS from Fig. 4.36
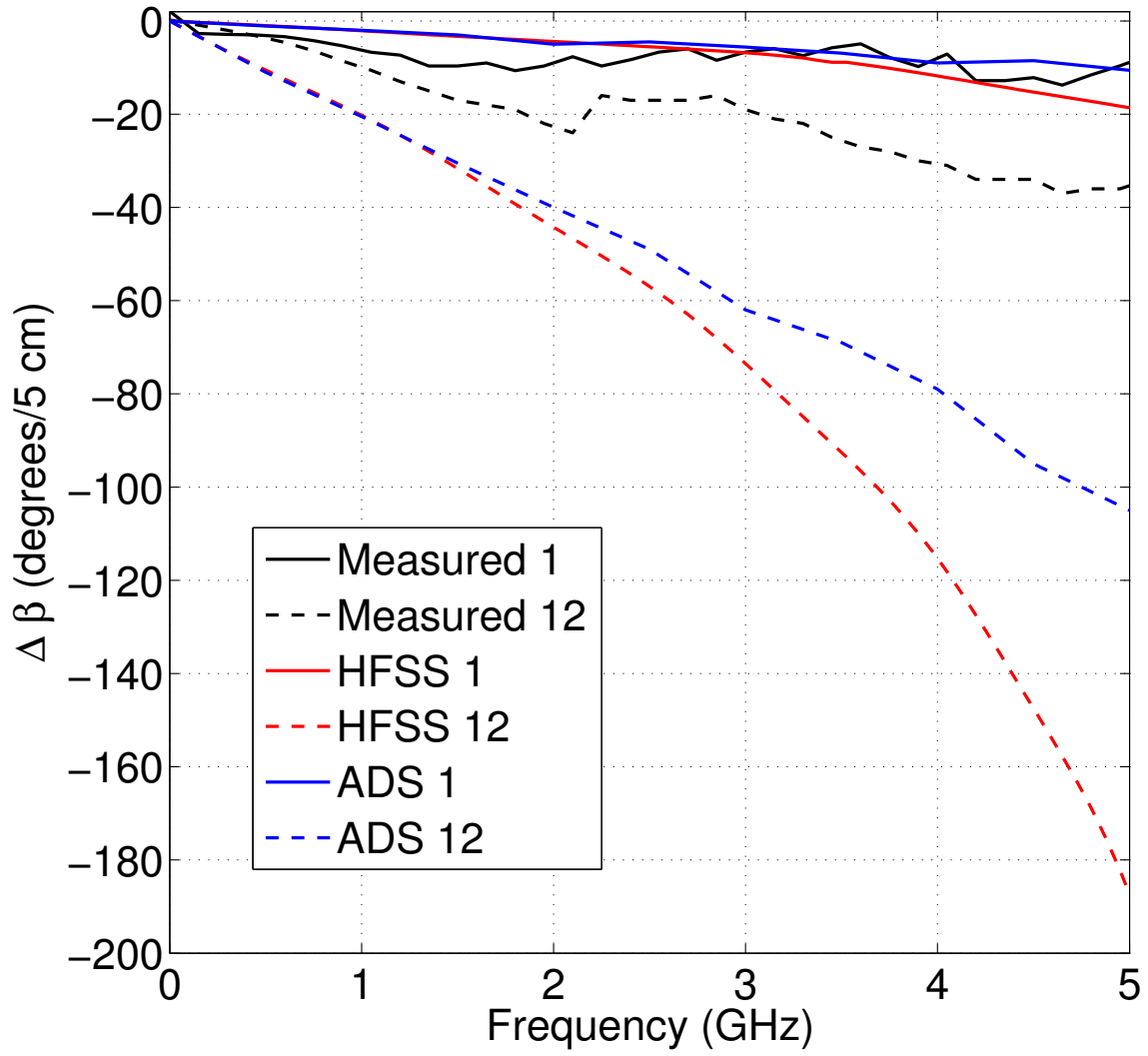
Figure A.7. Difference of β comparisons between ADS, HFSS, and Measurements from Fig. 4.51
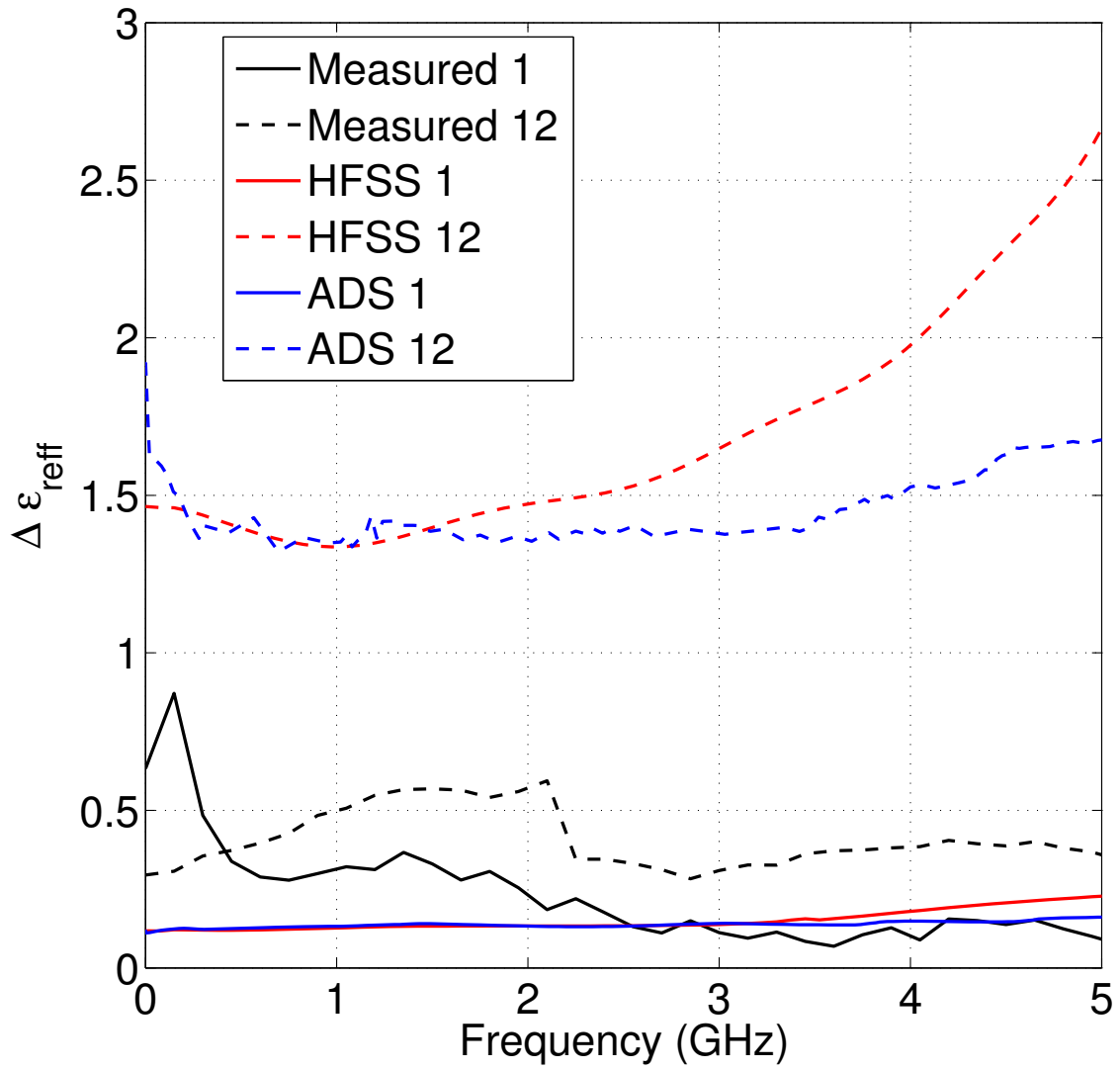
Figure A.8. Difference of ϵ_{reff} comparisons between ADS, HFSS, and Measurements from Fig. 4.52